JGR Atmospheres

RESEARCH ARTICLE
10.1029/2020JD034217

Special Section:
Atmospheric Rivers: Intersection of Weather and Climate

A Detailed, Multi-Scale Assessment of an Atmospheric River Event and Its Impact on Extreme Glacier Melt in the Southern Alps of New Zealand

Elena Kropač[1], Thomas Mölg[1], Nicolas J. Cullen[2], Emily Collier[3], Carolyne Pickler[1], and Jenny V. Turton[1]

[1]Climate System Research Group, Institute of Geography, Friedrich-Alexander University Erlangen-Nürnberg (FAU), Erlangen, Germany, [2]School of Geography, University of Otago, Dunedin, New Zealand, [3]Department of Atmospheric and Cryospheric Sciences (ACINN), University of Innsbruck, Innsbruck, Austria

Key Points:

- The mass balance of Brewster Glacier is affected by an atmospheric river causing extreme melt through rain and turbulent energy transfer
- Orographic enhancement and weak stability in the atmospheric river cause precipitation on windward slopes while leesides are foehn-affected
- Regional atmospheric modeling can advance the process understanding of the glacier-climate relationship in New Zealand's mountains

Correspondence to:
E. Kropač,
elena.kropac@fau.de

Citation:
Kropač, E., Mölg, T., Cullen, N. J., Collier, E., Pickler, C., & Turton, J. V. (2021). A detailed, multi-scale assessment of an atmospheric river event and its impact on extreme glacier melt in the Southern Alps of New Zealand. *Journal of Geophysical Research: Atmospheres*, *126*, e2020JD034217. https://doi.org/10.1029/2020JD034217

Received 12 NOV 2020
Accepted 31 MAR 2021

Abstract North-westerly airflow and associated atmospheric rivers (ARs) have been found to profoundly influence New Zealand's west coasts, by causing flooding, landslides and extreme ablation and accumulation on glaciers in the Southern Alps. However, the response of local glacier mass balance to synoptic-scale circulation, including events with ARs, has typically not been investigated by considering mesoscale processes explicitly. In this study, high-resolution atmospheric simulations from the Weather Research and Forecasting model are used to investigate the mesoscale drivers of an extreme ablation event on Brewster Glacier (Southern Alps), which occurred on February 6, 2011 during the landfall of an AR on the South Island. The following processes were found to be crucial for transferring the high temperature and water vapor contained in the AR into energy available for melt on Brewster Glacier: First, the moist-neutral character of the air mass enabled the flow to pass over the ridge, leading to the development of orographic clouds and precipitation on the windward side of the orography, and foehn winds on the leeside. These processes fueled melt through longwave radiation and strong turbulent and rain heat fluxes within the high-condensation environment of the orographic cloud. Second, orographic enhancement occurred due to both cellular convection within the cloud and the combined effect of multiple precipitating systems by the seeder-feeder-mechanism. These results indicate the potential importance of AR dynamics for New Zealand's glaciers. They also illustrate the benefit of mesoscale atmospheric modeling for advancing process understanding of the glacier-climate relationship in New Zealand.

Plain Language Summary Atmospheric rivers, which are elongated, narrow structures in the atmosphere that convey large amounts of moisture through the midlatitudes, have been found to impact coastal regions worldwide, including New Zealand. Besides causing flooding and landslides, they can affect glaciers in coastal mountains such as the Southern Alps. The processes causing the high temperature and moisture in atmospheric rivers to trigger melt (or snowfall) at the glacier surface have, however, not been investigated explicitly because they operate at the size of mountain valleys and ridges which are difficult to represent in global data-sets. We address this by using an atmospheric model with high spatial detail to simulate a case study, where an atmospheric river coincided with extreme melt on Brewster Glacier in the Southern Alps. We find that the stability characteristics of the impinging warm and moist air masses lent the air the potential to ascend the mountain instead of being directed around. This resulted in cloud and precipitation development on the windward slopes whereby rain amounts were further enhanced by internal processes within the clouds. Melt was promoted through heat released from condensation and rainfall. Conversely, on the lee slopes, downslope winds caused warm and dry conditions.

1. Introduction

Glaciers are recognized as useful indicators of global climate change, owing to the sensitivity of their mass balances to small changes in climate (Nye, 1960). Although there has been an overall negative trend in global glacier mass balance since the early 1990s, which has been attributed to anthropogenic warming (Marzeion et al., 2014), glacier responses differ regionally, with some glaciers in the Karakoram and Pamir (e.g., Gardelle et al., 2013), western Scandinavia (e.g., Trachsel & Nesje, 2015), southern Patagonia (e.g.,

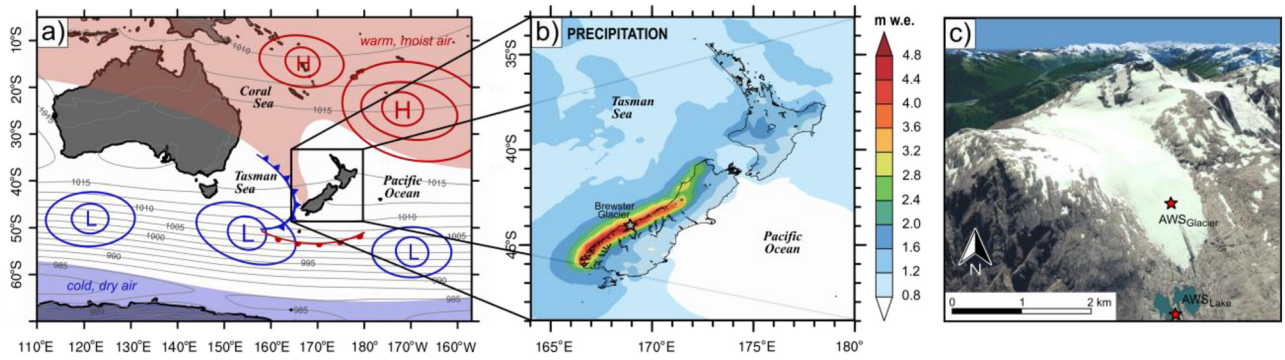

Figure 1. Climatological setting of New Zealand: (a) Geographic location in the south-west Pacific Ocean within the Southern Hemisphere westerly wind belt and embedded frontal activity. Gray contour lines show the mean sea level pressure (hPa) in 1989–2018, with the colored areas distinguishing between warm, moist air masses of the subtropical high-pressure belt in the north and cold, dry subpolar air in the south. The mechanism of how ARs are frequently advected toward the west coast of New Zealand (Prince et al., 2021) is indicated. (b) Distribution of mean annual precipitation (1989–2018) over New Zealand, demonstrating a west-east gradient across the South Island. Underlying data set for both (a) and (b) is the ERA5 reanalysis. (c) Quickbird image of Brewster Glacier from February 8, 2011 draped onto a 15-m resolution Digital Elevation Model (adapted from Sirguey et al., 2016, Figure 1), with locations of the two AWSs being indicated by the red markers. ARs, atmospheric rivers; AWSs, Automatic Weather Stations.

Braun et al., 2019; Schaefer et al., 2015), and New Zealand (e.g., Mackintosh et al., 2017) showing periods of stable or even positive mass balances. Although 15 of the 26 advancing glaciers observed worldwide in 2005 were located in New Zealand (WGMS, 2008), the overall volume of ice contained in the Southern Alps has decreased (Chinn et al., 2012) as the largest debris-covered glaciers (e.g., Tasman Glacier) continued to retreat. The advancement of the fast responding glaciers at this time was controlled primarily by discrete periods of low air temperature associated with anomalous southerly winds and low sea surface temperatures in the Tasman Sea region (Mackintosh et al., 2017). These contrasting glacier responses to climate forcing indicate the complexity of glacier-climate interactions in the Southern Alps and illustrate the need to further investigate the role of regional climate dynamics in this unique part of the world.

New Zealand is situated between 34° and 47°S in the open south-west Pacific Ocean, south of the quasi-stationary high-pressure belt of the subtropical Pacific and north of the polar air masses in the Southern Ocean. These contrasting air masses interact within the predominantly westerly airflow of the midlatitude storm track, which strongly controls the weather and climate of the South Island by the frequent passage of depressions and fronts (Figure 1a; Fitzharris, 2001). The frontal systems often involve atmospheric rivers (ARs), which are filamentary corridors of strong horizontal water vapor transport in the lower troposphere that are responsible for the bulk of the poleward movement of water vapor, sensible and latent heat across the midlatitudes (Zhu & Newell, 1998). They are typically associated with the low-level jet (LLJ) residing within the warm conveyor belt (WCB) ahead of the cold front in extratropical cyclones or midlatitude wave troughs (Ralph et al., 2018; Zhu & Newell, 1998). ARs have a bifold impact since they are both responsible for hazards and at the same time represent the main supplier of water resources in many coastal regions where they make landfall (Ralph & Dettinger, 2011). Due to New Zealand's exposed maritime midlatitude setting, ARs regularly impinge on the western coasts of the country (Waliser & Guan, 2017) where they have been linked to extreme precipitation events (Rosier et al., 2015), river flooding (Kingston et al., 2016) and glacial mass balance variability (Cullen et al., 2019; Little et al., 2019). The Southern Alps, running along the west coast of the South Island over a distance of 500 km, represent the country's most significant topographic feature with many peaks exceeding 2,500 m and the highest (Mt. Cook) extending to 3,724 m. Since their main axial range is oriented perpendicular (SW-NE) to the dominant Southern Hemisphere westerlies, they operate as an effective low-level barrier against the prevailing airflow and thus, substantially modify the synoptic-scale circulation (McCauley & Sturman, 1999). The frequent pile-up of air masses and associated development of extensive cloud and precipitation on their western (windward) side leads to the formation of a significant west-to-east precipitation gradient across the South Island, with large amounts of orographic precipitation on the west coast and in the mountains (3,000 to over 12,000 mm water equivalent [w.e.] a^{-1}) and a pronounced dry eastern side (<1,000 mm w.e. a^{-1}; Figure 1b; Griffiths & McSaveney, 1983). This input combined with simultaneously high melt rates in summer result in the glaciers having extremely

high mass turnover, causing them to be highly sensitive and adjust rapidly to climate forcing (Anderson & Mackintosh, 2012).

Many previous studies have investigated the micro- and large-scale controls on glacier mass balance in the Southern Alps. Energy balance and degree-day modeling approaches (e.g., Cullen & Conway, 2015; Gillett & Cullen, 2011; Hay & Fitzharris, 1988; Marcus et al., 1985; Neale & Fitzharris, 1997) facilitated the detailed assessment of some of the most significant factors governing local energy and mass balance within the surface boundary layer of glaciers and snow packs, including radiation (Conway et al., 2015), cloud cover (Conway & Cullen, 2016), and turbulent heat fluxes (Conway & Cullen, 2013). Examination of the relationship between local processes and larger-scale climate dynamics revealed that mass gains and losses are closely coupled with synoptic conditions in the Australia-New Zealand region (e.g., Clare et al., 2002; Fitzharris et al., 1997; Hay & Fitzharris, 1988; Neale & Fitzharris, 1997; Purdie et al., 2011), with both glacial ablation and accumulation tending to be linked to specific patterns of geostrophic flow and moisture advection (Cullen et al., 2019). In particular, ARs have been found to exert a key influence on glacial mass balance variability by manifesting both extreme snowfall and melt events (Little et al., 2019). Over a wider spatial and temporal perspective, the strength and frequency of synoptic weather systems and the direction of geostrophic flow are controlled by hemispheric and global modes of climate variability, teleconnection patterns and zonal wave activity; accordingly, glacier fluctuations and ice volume changes in the Southern Alps have been associated with numerous anomalies due to climate modes, such as the El Niño Southern Oscillation, the Southern Annular Mode, the Inter-decadal Pacific Oscillation as well as the Zonal Wave 3 and Pacific South American patterns (e.g., Fitzharris et al., 2007, 1992; Mackintosh et al., 2017; Salinger et al., 2019; Sirguey et al., 2016).

Despite a broad understanding of the influence of local- and large-scale atmospheric controls on glacier mass balance in the Southern Alps, the response of a glacier to climatic change is often subject to non-linear dynamics and topo-climatic effects on the scale of individual valleys and ridges. According to the concept of Mölg and Kaser (2011), the establishment of a direct (statistical) connection between large-scale climate fluctuations and local mass balance variability masks the mesoscale, orographically induced processes at play, which provide the physical link between the two distinct atmospheric scales and effectively convert the large-scale climatic signal into a "local footprint" of mass change. Given the continuous improvement and high standard of state-of-the-art atmospheric models, efforts to simulate mesoscale processes affecting glaciers in complex terrain have been successful in numerous studies, and dynamical downscaling has even served to obtain highly resolved records of local climate, thus enabling the direct coupling of atmospheric with energy and mass balance models (e.g., Collier et al., 2015; Mölg & Kaser, 2011; Schaefer et al., 2015). No dynamical downscaling approach has yet been employed to systematically disclose the full process chain conducive to mass changes on New Zealand glaciers.

We hypothesize that mesoscale processes, which are neglected by statistical downscaling, are essential for understanding how large-scale conditions impact local mass balance variability in the Southern Alps. Therefore, our objective is to resolve the mesoscale process space in the mountain's atmospheric boundary layer (ABL) above a New Zealand glacier for the first time by using a high-resolution atmospheric model. In this study, we implement a modeling case study of an AR event in 2011 that coincided with extreme ablation on Brewster Glacier in the Southern Alps. Our focus is motivated by previous work indicating that on Brewster Glacier (i) less frequent but large ablation events can account for almost 25% of total ablation during summer and are therefore particularly important for total mass loss (Gillett & Cullen, 2011), (ii) the majority of extreme ablation events in 2010–2012 have occurred during ARs (Little et al., 2019), and (iii) there is large uncertainty regarding the exact physical mechanisms of AR-related extreme precipitation and its impact on glacier mass balance. Given the uncertainties and the research gap outlined, our study yields the potential to increase the knowledge of how dynamical, thermodynamic and microphysical phenomena of the mountain-induced flow affect glacier mass balance and hence, provide a more comprehensive understanding of the glacier-climate relationship in the Southern Alps.

2. Data and Methods

2.1. Site Description

Brewster Glacier is a small maritime alpine glacier in the Mount Aspiring National Park located at 44.08°S, 169.43°E, just west of the Main Divide of the Southern Alps. The glacier covers an area of ~2 km^2 and descends the south-western slope of Mount Brewster (2,516 m), spanning a distance of ~2.5 km from a maximum elevation of 2,400–1,700 m a.s.l. While the lower and major part of the glacier (<2,000 m; 77% of total area) is gently southerly sloping (10° mean gradient), the upper and smaller part is steeply declining in a south-westerly direction (31° mean gradient) and contains a number of large ice cliffs (Figure 1c). Average meteorological conditions in the lower ablation zone of Brewster Glacier (~1,760 m; 820 hPa) are characterized by an annual mean temperature of 1.2°C and mean annual precipitation amounts of more than 6,100 mm w.e., with the majority of precipitation falling within a few degrees of the freezing level (Cullen & Conway, 2015). Note that the annual precipitation amounts recorded at Brewster Glacier are higher than can be represented by the relatively coarse-resolution reanalysis data for the Southern Alps in Figure 1b. The limited ability to capture localized precipitation maxima in mountainous regions is a widely observed shortcoming of ERA5 and other reanalyses (e.g., Sharifi et al., 2019).

Brewster Glacier is one of the best investigated glaciers in New Zealand with the longest in situ mass balance record of the Southern Alps. The record has been collected within the framework of a direct mass balance survey carried out since 2004, which involves the measurement of snow depth and density via snow pits and snow probing at the end of the accumulation season (April–October) and the determination of surface height change from ablation stakes at the end of the ablation season (November–March). The glaciological measurements are supplemented by a comprehensive aerial survey using oblique aerial photography, which has been carried out since 1977 (Chinn et al., 2005, 2012). Brewster Glacier thereby represents 1 of 50 index glaciers in the Southern Alps permanently surveyed by flyovers. The photographs enable the delineation of the end of summer snowlines, which have been used as a proxy for equilibrium line altitudes. Calculating their departure from the long-term equilibrium line altitude permits inference of annual mass balances (e.g., Chinn et al., 2005; Sirguey et al., 2016) and volume changes (e.g., Chinn et al., 2012; Salinger et al., 2019) of glaciers in the Southern Alps. Since 2004, permanent observations of the near-surface meteorological conditions in the immediate surrounding of Brewster Glacier are available from an Automatic Weather Station (AWS) installed on bare rock, ~200 m from the glacier tongue beside a proglacial lake at 1,650 m a.s.l. (hereafter AWS_{Lake}; Figure 1c; Cullen & Conway, 2015; Gillett & Cullen, 2011).

Importantly, due to its moderate elevation (Hoelzle et al., 2007), its central position close to the Main Divide near the midpoint of the north-south distribution of glaciers in the Southern Alps (Chinn et al., 2012) and its relatively high exposure to synoptic weather systems, Brewster Glacier is representative of glacier surface climate and (historical) mass balance variability in the wider Southern Alps region (Salinger et al., 2019; Willsman et al., 2015), thereby reflecting the typical glacier response to regional and large-scale ocean-atmosphere dynamics.

2.2. Glacier-Scale Meteorological, Energy and Mass Balance Data

A 22-month period from October 25, 2010 to September 1, 2012 served as the investigation period. During this time, a combined measurement campaign and mass and energy balance study was carried out at a site in the ablation zone of Brewster Glacier (1,760 m a.s.l.; Figure 1c), including high-resolution (30 min) meteorological measurements obtained at an on-glacier AWS ($AWS_{Glacier}$) as well as comprehensive mass and energy balance modeling. The meteorological variables recorded at $AWS_{Glacier}$ include air temperature (T_a), relative humidity (RH), air pressure (P), wind speed (U), incoming ($SW\downarrow$) and outgoing ($SW\uparrow$) shortwave radiation, incoming longwave radiation ($LW\downarrow$), and surface temperature. Precipitation data ($PREC$) were not available and were therefore the only variable sourced from the AWS_{Lake}. The data were corrected for undercatch with a factor of 1.25, compressed to 6-h totals and complemented with winter precipitation by incorporating extrapolated measurements from a valley station in Makarora (Cullen & Conway, 2015). For a full documentation of the instruments at both AWSs and the data treatment, see Cullen and Conway (2015). The meteorological data collected at $AWS_{Glacier}$ were used to force a combined mass and energy balance model (Mölg et al., 2008, 2009) in order to obtain a detailed breakdown of the glacier surface

energy and mass balance (SEB and SMB) at the $AWS_{Glacier}$ site. A precise description of the model configuration and evaluation of the data output over the 22-month period (2010–2012) is provided by Conway and Cullen (2016) and Cullen and Conway (2015). Additional information about the turbulent heat flux and radiation schemes developed for the modeling can be found in Conway and Cullen (2013) and Conway et al. (2015), respectively. Overall, the model was found to realistically simulate all relevant surface energy fluxes and to successfully reproduce the accumulated mass balance throughout the simulation period, including individual large ablation and snowfall events (Conway & Cullen, 2016).

2.3. Reanalysis Data

For the representation of the synoptic-scale conditions, we used the ERA5 data set (Hersbach et al., 2020) from the European Center for Medium-Range Weather Forecasts, as it is the most highly resolved global reanalysis available, providing atmospheric, land surface and ocean variables at a 31 km horizontal grid spacing, 137 vertical levels reaching up to 0.01 hPa and an hourly output frequency. ERA5 has been successfully used for a range of applications in climate research and has been shown to yield an overall good performance and improvement compared to previous versions and other reanalysis products (e.g., Albergel et al., 2018; Olauson, 2018).

2.4. Selection and Investigation of the Case Study

For the selection of a case study day, we rely on existing work. Little et al. (2019) identified extreme ablation events from SMB modeling, defined as the 10 highest average ablation days during their study period (2010–2012), and examined the associated synoptic-scale situation as well as the micro-scale meteorological conditions and energy budget at the glacier surface. The six highest ablation events (all in summer) were found to be dominated by north-westerly circulation, locally associated with anomalously high air temperatures and rainfall amounts, prompting melt through high sensible, latent and rain heat fluxes, and additional energy input from longwave radiation. The importance of north-westerly flow in driving high ablation on Brewster Glacier was also highlighted by Cullen et al. (2019) who investigated the relationship between glacial mass balance variability and synoptic weather types. Prince (2020) found that five out of the six highest melt events on Brewster Glacier involved the highest category ARs (categories 4 and 5), based on the strength of the damage when they made landfall. Categories 4 and 5 correspond to "mostly hazardous, also beneficial" and "primarily hazardous" events with >1,000 to >1,250 kg m^{-1} s^{-1} totals of column integrated water vapor transport (IVT; Ralph et al., 2019).

Based on these findings, we selected February 6, 2011 as a case study for mesoscale investigation since: It is characterized by local- and synoptic-scale conditions that are typical during extreme ablation on Brewster Glacier; it has a strong AR detected; and it exhibits the strongest melt event in the 2010–2012 period.

To provide the framework for the mesoscale analysis and to link processes operating at the large and local atmospheric scales, we analyzed the case study event concerning (i) the related synoptic-scale atmospheric circulation and moisture fluxes, and (ii) the micro-scale glacial climatic environment and SEB. For (i) we used ERA5 atmospheric fields of surface pressure, column integrated water vapor (IWV), IVT, vector wind (at 10 m) as well as synoptic charts from MetService New Zealand, issued at 00:00 UTC on February 5 and 6, 2011, respectively. For (ii) we utilized data from $AWS_{Glacier}$ (with precipitation from AWS_{Lake}) and the SEB modeling (Conway & Cullen, 2016; Cullen & Conway, 2015), which reflect the meteorological conditions and mass and energy fluxes at the glacier surface, respectively.

2.5. Atmospheric Modeling

A high-resolution simulation of the atmospheric processes during the case study was performed with the advanced research version of the Weather Research and Forecasting (WRF) model (Skamarock et al., 2019) v. 4.0.1. The simulation was set up with two one-way nested domains centered over New Zealand and the Southern Alps region (Figure 2a; Table 1), allowing for telescoping horizontal grid spacing from 6 km in the parent domain (D1) to 2 km in the region of interest (D2). The resolution of the inner domain ensures that Brewster Glacier (covering an area of ~2 km^2) is represented explicitly by one land-ice grid point. In the

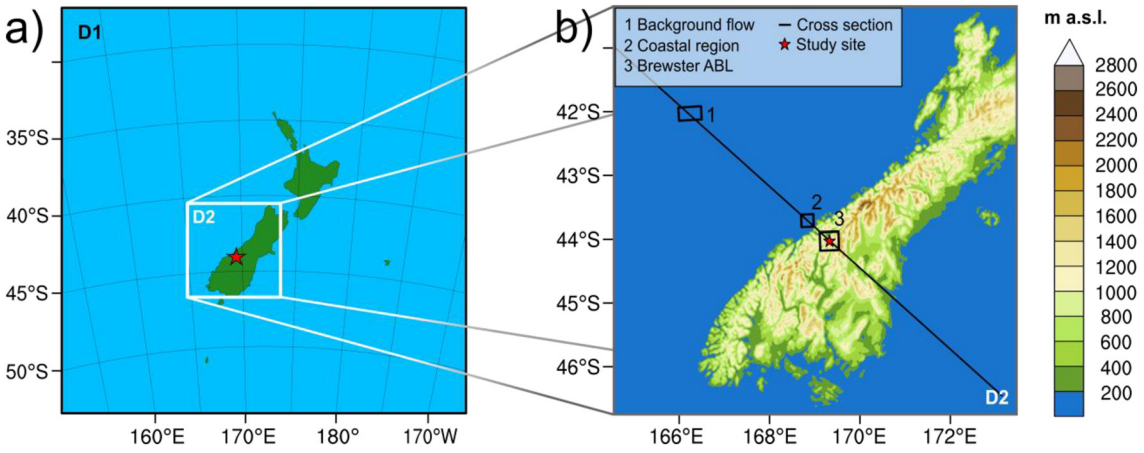

Figure 2. (a) Domain configuration used in the study (cf. Table 1); (b) WRF D2 topography and locations selected for analysis (cf. Section 2.6). WRF, Weather Research and Forecasting.

vertical, 84 model levels were specified, with the model top located at 50 hPa and the lowest eta-level corresponding to ~9 m above ground. In the coarse-resolution domain (D1), the model was forced at the lateral boundaries with ERA5 reanalysis data, while evolving meteorological conditions (wind, potential temperature and vapor mixing ratio) were nudged toward the input in all atmospheric layers at hourly frequency. The model simulation was initiated 3 days (72 h) prior to the event day (00:00 on February 3, 2011) and finished 12 h after the event day (12:00 on February 7, 2011). The first 48 h were discarded for model spin up, providing the next 60 h (00:00 on February 5 to 12:00 on February 7) for model evaluation and analysis of mesoscale processes. Note that all times are in New Zealand Standard Time (NZST; UTC+12). The output interval was defined as 3-hourly for D1 and hourly for D2.

Table 1
Summary of the Most Relevant WRF Model Settings Used in This Study Concerning Domain Configuration, Physics and Dynamics Options, and Forcing Data

Domain configuration	
Horizontal grid spacing	6 km (D1) and 2 km (D2)
Grid dimensions	500 × 500 and 346 × 346
Time step	30 and 10 s
Vertical levels	84; lowest eta-level: 0.997769 (~9 m above ground)
Model top pressure	5,000 Pa
Model physics	
Microphysics	Morrison 2-moment (Morrison et al., 2009)
Cumulus	Kain-Fritsch (Kain, 2004); none in D2
Radiation	Shortwave: Dudhia (Dudhia, 1989); Longwave: RRTMG (Iacono et al., 2008)
Planetary boundary layer	YSU (Hong et al., 2006)
Atmospheric surface layer	Monin-Obukhov (revised MM5; Jiménez et al., 2012)
Land surface model	Noah-MP (Niu et al., 2011)
Dynamics	
Top boundary condition	w-Rayleigh damping
Diffusion	Calculated in physical space
Lateral boundaries	
Forcing	ERA5 reanalysis 31 × 31 km, hourly (Hersbach et al., 2020)
Grid nudging	Only in D1; hourly frequency; default nudging coefficient used (0.0003 s^{-1})

The physics and dynamics settings used in this study are based on our experience using WRF in diverse latitudinal, topographic and climatic environments (e.g., Collier & Immerzeel, 2015; Mölg & Kaser, 2011; Turton et al., 2020). We selected the best performing configuration (in terms of statistical performance metrics) out of a set of 45 sensitivity runs involving different combinations of physics und dynamics options as well as nudging techniques and time step settings. The resulting set up (Table 1) is similar to one that has been successfully applied to Southern Patagonia (Sauter, 2020), a similar climatic setting as New Zealand. For the high-resolution domain (D2), topographic effects on radiation, including both topographic shading and slope effects, were accounted for and a cumulus parameterization was neglected since model simulations using a grid spacing smaller than 4 km are considered to resolve most convective processes explicitly (Weisman et al., 1997). Cloud microphysics were represented by the Morrison 2-moment scheme, which we consider the most robust parametrization scheme for clouds and precipitation in high-mountain and/or glacierized environments based on our previous modeling studies in different climatic zones (e.g., Collier et al., 2018; Mölg et al., 2017; Temme et al., 2020; Turton et al., 2020). Specifically, in the Himalayas, the Morrison 2-moment scheme has been proven to produce the most accurate output (compared to other microphysics schemes) when evaluated against observational data and radar/lidar cloud products (Orr et al., 2017). The scheme also outperformed other microphysics parameterizations tested during our sensitivity runs in terms of modeled precipitation amounts at the glacier site.

For both domains, land use came from the default, Moderate Resolution Imaging Spectroradiometer (MODIS)-based land-cover data set with a resolution of 30 arc seconds (~1 km); in case of topography, NASA Shuttle Radar Topography Mission (SRTM) version 4.1 data (Jarvis et al., 2008) resampled to a 1 km grid were ingested (e.g., Collier et al. 2018). To ensure the correct spatial classification of snow- and ice-covered surfaces, the WRF land-ice mask and associated soil categories and vegetation parameters were updated by incorporating recent glacier extent data from the Randolph Glacier Inventory (RGI; Pfeffer et al., 2014) v. 6.0 (e.g., Collier et al., 2015). Furthermore, the terrain height of the grid cell including $AWS_{Glacier}$ was manually decreased by 94 m, to match observations and to enable direct comparability between WRF output and local measurements. The change is unlikely to affect the atmospheric simulation in a disadvantageous or unrealistic manner as (i) the relative topography pattern in the region was retained, and (ii) the specification resulted in a reduced altitude difference to adjacent grid cells thus minimizing the risk of numerical instability (Zängl, 2012). Following Collier et al. (2018), to further optimize the representation of glacier surfaces in the Noah-MP land surface model, we removed the minimum snow depth to permit exposed ice and decreased the lower bound for surface albedo, to 0.47, which corresponds to the average albedo prevailing on Brewster Glacier on days without snow cover in the study period (e.g., Cullen & Conway, 2015).

Since the study focuses on Brewster Glacier, WRF modeled surface variables were evaluated against measurements obtained at $AWS_{Glacier}$ by applying statistical performance metrics including root mean square error (RMSE), mean model bias (MMB) and Pearson Correlation Coefficient (r). Meteorological variables considered correspond to those outlined in Section 2.2, plus specific humidity (q) which was calculated from T_a, RH, and P. Of the (sensor-) height-dependent variables (T_a, RH, q, and U), air temperature and humidity (2 m) are directly comparable to WRF output, while for wind speed there is a discrepancy in reference heights, as U corresponds to a fixed height of 10 m in the WRF model but was recorded at a variable instrument height (between 2.5 and 3.4 m) at the AWS site. We therefore scaled measured U to 10 m by applying a logarithmic wind profile that accounts for atmospheric stability (e.g., Andreas et al., 2006), with friction velocity sourced from a version of the SEB data set (Cullen & Conway, 2015) that used the $c_{z/L}$-parametrization to calculate turbulent heat fluxes (Conway & Cullen, 2013).

2.6. Mesoscale Analysis

To capture the nature and evolution of mesoscale processes, we investigated three separate aspects: the undisturbed ("background") flow approaching the mountain range from the north-west; the changes in air mass and flow regime characteristics due to orographic effects when the air impinges on the mountains; and the resulting conditions in the mesoscale region and ABL above Brewster Glacier, which eventually impact the glacier surface by the continuous exchange of energy, momentum and mass at the glacier surface.

The background flow was examined by assessing vertical profiles of atmospheric stability, humidity and flow regime parameters averaged over a 20 × 20 km (100 grid points)-sized region ~250 km upstream of the

Southern Alps (Figure 2b), which corresponds to the approximate Rossby radius of deformation indicating the offshore distance of orographic wind field modification (Overland & Bond, 1995). Static stability of the air was represented by both the dry and saturated squared Brunt-Väisälä-Frequencies (BVF), N^2, and N_m^2, respectively (Durran & Klemp, 1982; Equations 1b and 36). In contrast to the unsaturated BVF, N_m^2 accounts for the latent heat released from condensation in a saturated environment and was used because the lower and mid-levels of the upstream flow were often largely saturated or likely to reach saturation on their path toward the Southern Alps. To determine the presumable flow regime (blocking vs. overflow) of the bulk low-level (1,000–800 hPa) upwind flow, the Froude Number $Fr = U/Nh$ (Smith, 1980) was calculated, with h representing the height of the mountains (1,950 m). For U, we used the total wind (not the wind component normal to the ridgeline) as this was nearly perpendicular to the mountain range throughout the case study. Again, to account for the buoyancy-promoting effects of high low-level moisture content, we calculated a dry and moist version of Fr using N and N_m, respectively.

The modification of the airflow (concerning flow regime and air mass properties) through its encounter with the mountain chain was analyzed by vertical cross sectioning of stability and humidity metrics along a profile that runs along the axis of the approaching north-westerly (~310°) airflow and intersects the Southern Alps almost perpendicularly (Figure 2b). At each end of the cross section, 10 grid cells were considered as boundary zone (interface to D1) and therefore truncated. The behavior of the low-level wind field and the spatial change of surface variables (T_a, RH, $PREC$, U at the lowest eta-level) were further investigated within a region immediately upwind of the coast (20 × 20 km/100 grid points; Figure 2b) and by using two-dimensional-maps covering the full high-resolution model domain, respectively.

Atmospheric dynamics in the ABL above Brewster Glacier were examined in a region comprising 225 grid points (30 × 30 km) enclosing the glacier's immediate mountainous environment near the Main Divide (Figure 2b). We focused on the (vertical) structure and hydrometeor composition of clouds and the associated type and phase of precipitation. Cloud stability was represented by the saturated BVF (N_m^2) and hydrometeors, including cloud water, ice, snow, hail, graupel, and rain. The assessed variables were spatially averaged over the analysis region (Figure 2b).

3. Results and Discussion

3.1. Model Evaluation

Overall, the atmospheric model realistically captures the properties of the near-surface atmospheric environment at Brewster Glacier, with the bulk of modeled meteorological variables coinciding well with observations (Figure 3). In particular, air pressure and both long- and shortwave incoming radiation are simulated with very high accuracy concerning both diurnal cycles and absolute values ($r = 0.69$–0.98; MMB and RMSE < 1 hPa for P and <17 and 74 W m^{-2} for $LW\downarrow$ and $SW\downarrow$, respectively). For air temperature, precipitation, specific humidity and wind speed, temporal variability is well simulated ($r \geq 0.74$; 0.47 for $PREC$), but there are deviations in magnitudes. In the case of precipitation, the comparison with measured amounts of $PREC$ is not very straightforward because of (i) the coarse availability of the data in 6-hourly resolution bins (see Section 2.2), (ii) the measurements being sourced from AWS_{Lake} which is located 110 m below the glacier station, and (iii) contamination of the data with a 25% uncertainty range owing to general gauge undercatch. Model performance is poor in case of U and T_a, with the model producing a substantial overprediction of wind speed (MMB = 7.87 m s^{-1}) and an underestimation of air temperature (MMB = −2.45°C). Likewise, RH shows weak statistical metrics, which is mainly attributable to the fact that the air is permanently saturated in the model, while there is moist but still unsaturated variability in the observations, and to the negative bias in T_a associated with a reduced water holding capacity of the air.

We investigated possible culprits for the weak model performance in terms of wind speed in our study (including observational data used for evaluation, ERA5 driving data, model resolution, physical parametrizations) and conclude that the positive wind speed bias most likely arises from a combination of the following factors: (i) the difference in reference heights of the wind sensor and the model output which could not be reliably compensated by upscaling measured U, and (ii) the subgrid-scale influence of topography and local processes that may not be fully resolved at 2 km grid spacing. A partitioning of the total U error into u- and v-components showed that the largest overestimations by WRF coincide with very high v-winds, suggesting

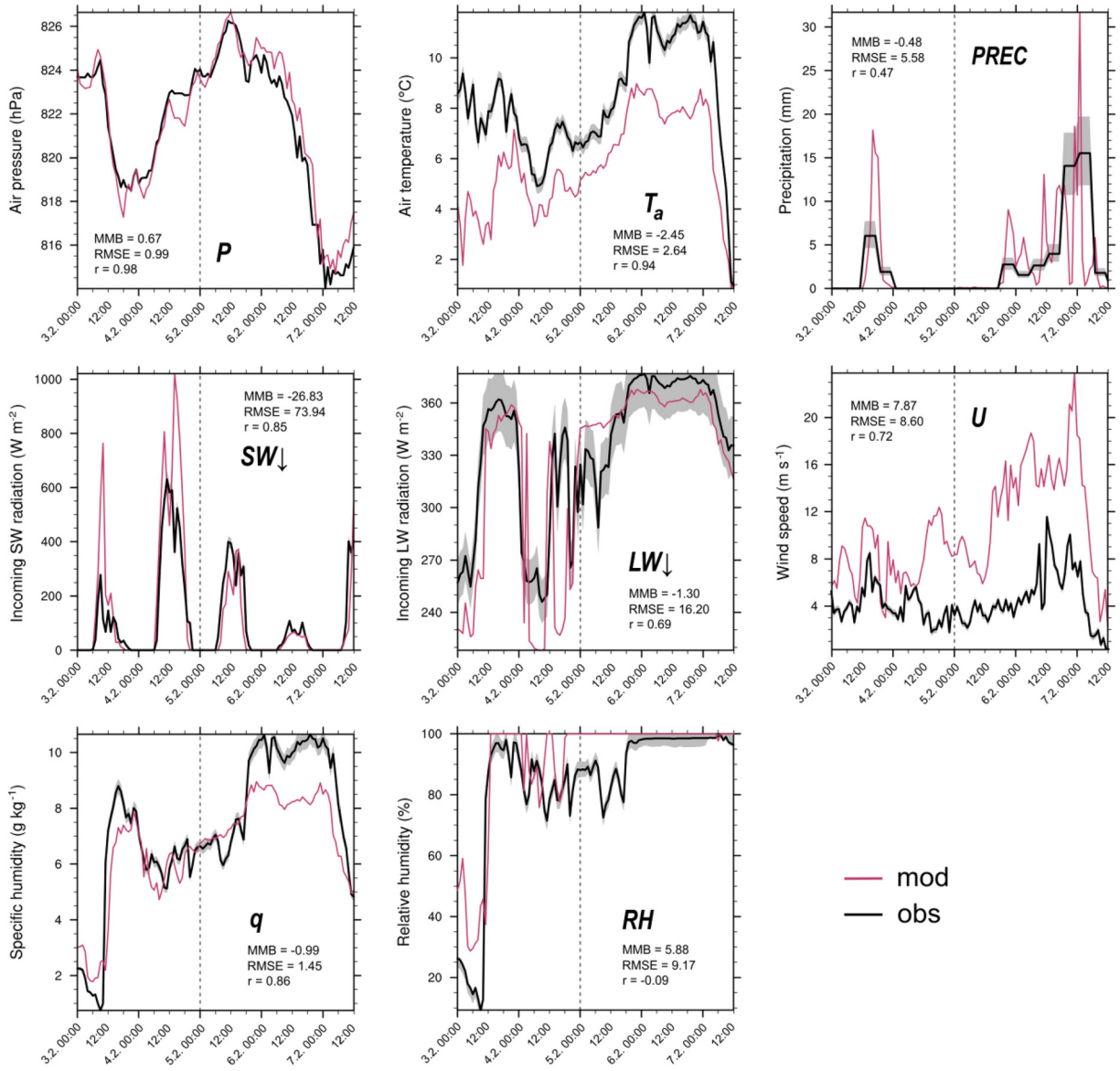

Figure 3. Comparison of modeled hourly meteorological surface variables with measurements from $AWS_{Glacier}$ (AWS_{Lake} for precipitation). The measurement uncertainty is indicated for each variable by the gray shading. Dashed gray lines separate the model spin-up time (first 48 h) from the evaluation period. Statistical performance metrics for the evaluation period are indicated, with MMB and RMSE given in the unit of the respective variable. Note that the precipitation is provided hourly by WRF but is only available in 6-hourly resolution bins in the case of observations.

that localized, terrain-induced flow features like flow reversal and/or downslope acceleration may have produced peaks that do not align with observations. Both wind speed overestimation and cold temperature biases in WRF are frequently reported phenomena, particularly with respect to locations situated in remote regions or within complex terrain (e.g., Gómez-Navarro et al., 2015; Temme et al., 2020; Zhang et al., 2013).

Despite these deficiencies, the statistical performance metrics are in the typical range of reported values for model evaluations of WRF based on hourly data (e.g., Bannister & King, 2015; Collier et al., 2018; Collier & Immerzeel, 2015; Temme et al., 2020) and are thus considered to be a reliable and appropriate basis for mesoscale investigations.

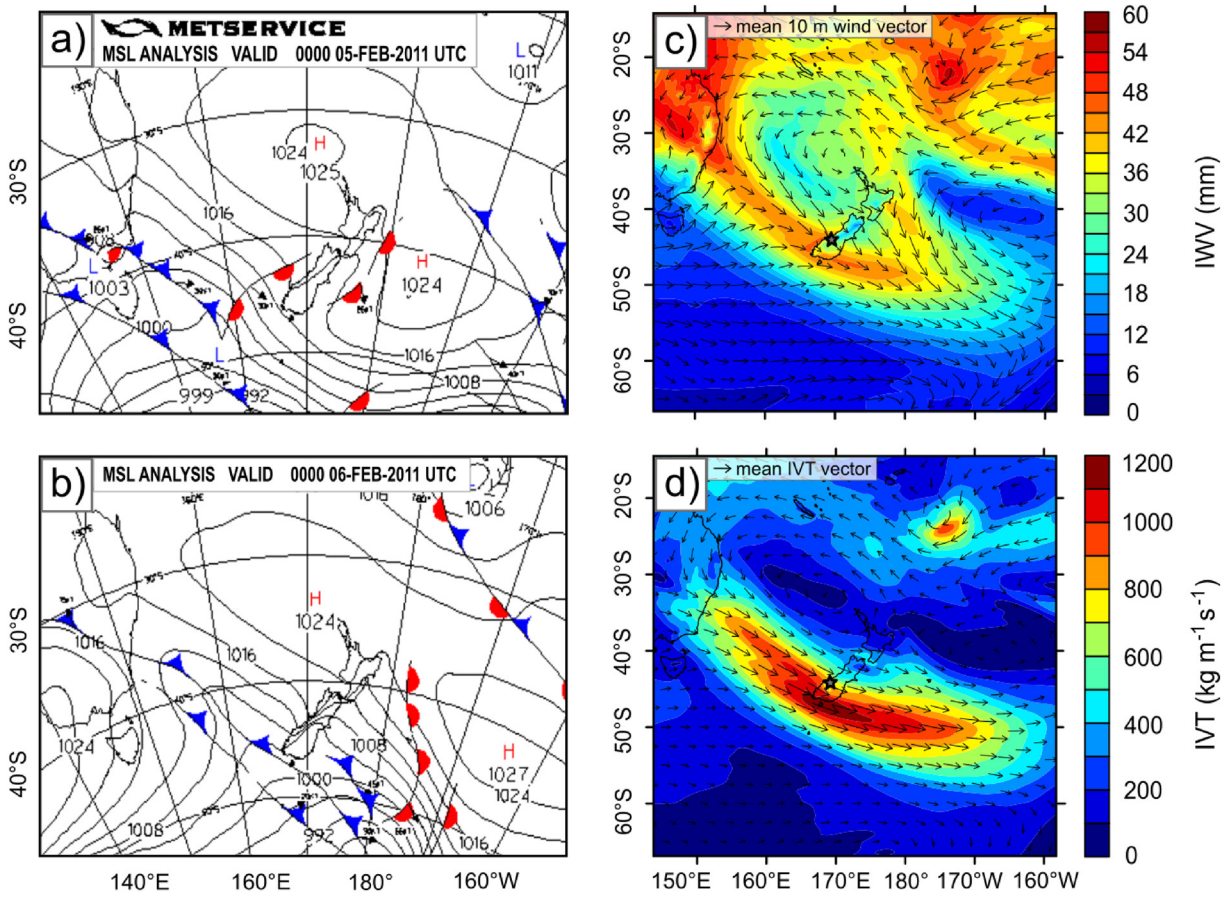

Figure 4. Synoptic-scale situation characterizing the case study: Synoptic charts for (a) February 5, 2011 and (b) February 6, 2011, issued at 12:00 NZST (note the time difference between UTC and NZST) by MetService New Zealand, with pressure centers and fronts mapped; average ERA5 (c) column integrated water vapor and (d) column integrated water vapor transport of the pre-cold-frontal AR during the event day (00:00 on February 6, to 00:00 on February 7, 2011). AR, atmospheric river.

3.2. Large-Scale Conditions

The event on February 6, 2011 occurs alongside a NE-SW pressure gradient formed by a large, elongated sub-tropical high-pressure system situated east of Australia and to the north-east of New Zealand, and low pressure located to the south-west of the South Island. The latter is related to the onset of an upper-level westerly trough coupled with a near-surface extratropical cyclone that has a cold front embedded (Figure 4b). The cyclone induces north-westerly airflow at its north-eastern flank, which effectively advects warm and moisture-laden air from the northern Tasman Sea region toward the Southern Alps. This air overrides the prevailing colder air, thereby establishing a warm front, which passes the study region prior to the event day at 14:00 on February 5, 2011 (Figure 4a). Moisture is transported in a narrow corridor by the LLJ embedded within the succeeding WCB of the cyclone, resulting in average IWV amounts of up to 48 mm (Figure 4c) and IVT totals of ~1,200 kg m^{-1} s^{-1} to the south-west and -east of the South Island (Figure 4d). These values considerably exceed the minimum thresholds defined for ARs (20 mm and 250 kg m^{-1} s^{-1}, respectively; Gimeno et al., 2014), thus suggesting the presence of a pre-cold-frontal AR. Indeed, the moisture plume was detected as an AR by Prince (2020) who recently obtained a 40-year climatology of ARs in the New Zealand region (Prince et al., 2021) based on detection and classification techniques developed by Guan and Waliser (2015) and Ralph et al. (2019), respectively. According to this categorization the AR on February 6, 2011 was ranked as an "exceptional" AR with "mostly hazardous, also beneficial" effects (Category 4 of 5; Prince, 2020). The AR initially passes around the south-western tip of the South Island with its core zone (region of maximum IVT in Figure 4d) making landfall in Fjordland and the coastal regions to the west of Brewster Glacier being affected by the broad mid-to-outer AR section. With the cold front

Table 2
The SEB Terms at $AWS_{Glacier}$ During the Case Study Compared to the Average Summer Ablation Period (DJF) at Brewster Glacier in 2010–2012 in Absolute and Relative (% of Q_M) Terms

Flux (W m^{-2})	February 6, 2011	DJF	Description
Q_M	456	171	Energy available for melt at the glacier surface: Sum of Q^*, Q_S, Q_L, Q_{RAIN} and a subsurface term (conductive heat flux, not shown), provided that the surface temperature is at 0°C
Q_S	140 (31%)	39 (23%)	Turbulent sensible heat flux
Q_L	168 (37%)	22 (13%)	Turbulent latent heat flux
Q_{RAIN}	76 (17%)	6 (4%)	Rain heat flux
Q^*	71 (16%)	106 (62%)	Net radiation: Budget of net shortwave (SW_{NET}) and net longwave (LW_{NET}) radiation fluxes
SW_{NET}	14 (20% of Q^*)	111 (105% of Q^*)	Net shortwave radiation flux: Balance of incoming shortwave ($SW\downarrow$) and outgoing shortwave ($SW\uparrow$) flux components
LW_{NET}	57 (80% of Q^*)	−6 (−5% of Q^*)	Net longwave radiation flux: Balance of incoming longwave ($LW\downarrow$) and outgoing longwave ($LW\uparrow$) flux components

Note. The energy balance terms listed (Q^*, Q_S, Q_L, Q_{RAIN}) do not comprise a full budget since the conductive heat flux from the subsurface is not included. During the case study and on average during the DJF period, however, this flux is negligibly small (−0.3% to −1 % of Q_M). Further note that energy fluxes toward (away from) the glacier surface are positive (negative), following the glaciological definition.

and associated AR moving north-eastward with time, Brewster Glacier becomes affected by the (slightly weakened) AR core by 00:00 on February 7, 2011. Daily average IVT experienced at locations offshore of Brewster Glacier reaches 750–1,000 kg m^{-1} s^{-1} (Figure 4c). The observed strength (moisture content and transport rate) of the event is consistent with findings reported by Little et al. (2019) and Prince (2020) who studied the AR based on ERA-Interim data. The impact of the AR ceases with the passage of the cold front at 00:00 on February 7, 2011, resulting in Brewster Glacier being dominated by south-westerly winds and postfrontal, cold and showery conditions (not shown).

The synoptic-scale atmospheric conditions during the event reflect the typical structure and sequence of a passing westerly trough and associated NW-SE-oriented front over the South Island and the Southern Alps (e.g., Wratt et al., 1996). This synoptic situation and related north-westerly airflow were considered essential for ARs to be advected toward the South Island west coast (Prince et al., 2021); they were also found to be predominant during extreme rainfall and river flooding events in the Southern Alps (Katzfey, 1995; Kingston et al., 2016), as well as to enhance melt on alpine glaciers (Hay & Fitzharris, 1988; Cullen et al., 2019; Gillet & Cullen, 2011; Little et al., 2019) and snow fields (Neale & Fitzharris, 1997).

3.3. Micro-Scale Conditions

The micro-scale conditions at the glacier surface were examined using meteorological measurements and energy balance terms (from the SEB modeling) at $AWS_{Glacier}$. A detailing of the surface energy budget including a description of the different SEB components is given in Table 2.

On the local scale, the case study on February 6, 2011 is characterized by anomalously warm and moist atmospheric conditions, with measured average air temperatures of 11.5°C, vapor pressure (e_a) of 13.4 hPa and precipitation totals of 133.4 mm w.e. d^{-1}. These values substantially exceed the respective averages of 5.1°C, 7.4 hPa, and 15.3 mm w.e. d^{-1} occurring during summer (December–February) ablation in the 2010–2012 period, with T_a and e_a being double and precipitation eight times as high as normal. Observed wind speeds (5.4 m s^{-1}) are also significantly enhanced compared to the DJF-average (3.2 m s^{-1}). These conditions enable anomalously large amounts of melt energy (Q_M; 455.5 W m^{-2}), resulting in high ablation rates at the glacier surface and a total mass loss of 117.8 mm w.e. at $AWS_{Glacier}$. In contrast, during average summer ablation, melt rates usually amount to 35.0 mm w.e. d^{-1} with a mean available Q_M of 170.5 W m^{-2} (Table 2). On average, Q_M is mainly (by 62%) provided by net radiation (Q^*) while the latent and rain heat fluxes (13% and 4%, respectively) play a less important role. Conversely, during the extreme melt event on February 6, 2011, enhanced U, T_a and atmospheric moisture result in the turbulent sensible (31%; Q_S) and

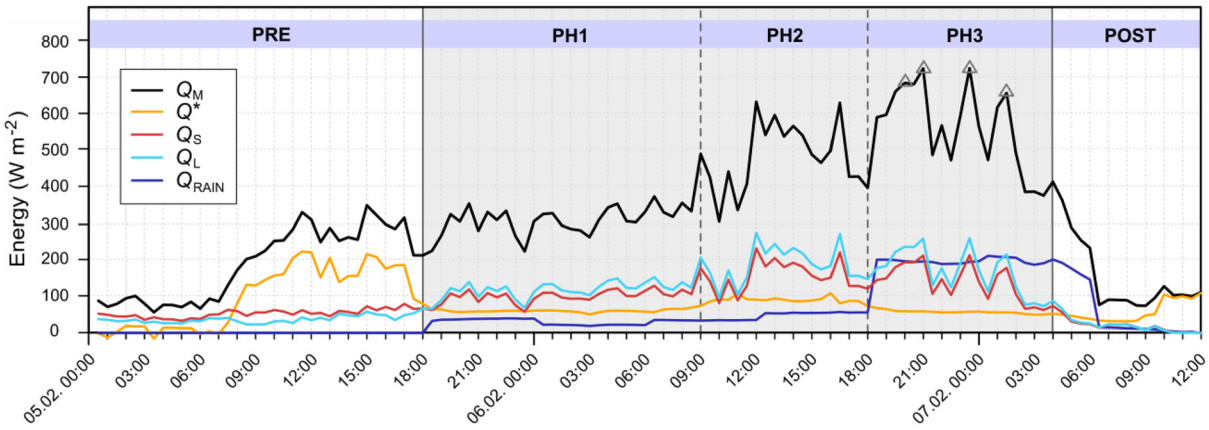

Figure 5. Temporal evolution of energy balance components before, during and after the melt event on February 6, 2011. Main stages are defined as: Pre-event conditions (PRE) before 18:00 on February 5; the actual melt event (gray shading) from 18:00 on February 5 to 04:00 on February 7 with sub-phases (PH1, PH2 and PH3) delimited by the dashed lines; post-event conditions (POST) from 04:00 on February 7 onwards. Gray triangles indicate times of peak melt. Positive (negative) energy fluxes are directed toward (away from) the surface.

latent (37%; Q_L) heat fluxes being the primary drivers, complemented by high amounts of heat released from rain (17%; Q_{RAIN}). Compared with clear-sky conditions, Q^* during the event accounts for only 16% of Q_M, with the major share of the reduced radiative energy being provided by net longwave radiation (80% of Q^*). Comparable contributions of convective and rain heat fluxes to melt energy during extreme melt events on Brewster Glacier have been found by Gillett and Cullen (2011) for summer 2007/2008. Also, previous research has emphasized the important role of heavy rainfall and turbulent heat fluxes for high ablation on other glaciers in the Southern Alps (Hay & Fitzharris, 1988; Purdie et al., 2008).

Investigation of the melt event on February 6 is extended from February 5 to February 7 and is subdivided into three stages reflecting pre-event- (PRE), event- and post-event- (POST) conditions (Figure 5): during pre-event conditions, air temperature and vapor pressure are already elevated compared to average DJF conditions, the air is moist but unsaturated, and there are moderate amounts of $LW\downarrow$ and $SW\downarrow$, pointing to changeable conditions with partially cloud-covered sky (cf. Figure 3). Melt energy is mainly provided by Q^* (52%), thus resembling usual summer ablation conditions driven by net shortwave radiation (84% of Q^*). Both a sharp rise in T_a of more than two degrees, with associated increases of e_a, $LW\downarrow$, U and RH, and the onset of precipitation at around 18:00 on February 5 mark the beginning of the melt event (cf. Figure 3). Until about 09:00 on February 6 (PH1), turbulent fluxes (71% of Q_M), with additional energy from Q^* (19%) and Q_{RAIN} (10%) which are provided by high $LW\downarrow$ and moderate amounts of liquid precipitation, respectively, (over-) compensate the lack of melt energy from $SW\downarrow$ during nighttime, thus causing a slight rise of Q_M. As of 09:00 (PH2), increasing precipitation and a marked enhancement of wind speed (cf. Figure 3), associated with an intensification of turbulent heat fluxes, cause a strong increase of melt energy; relative contributions to Q_M thereby remain largely unchanged. At around 18:00 (PH3), heavy rain and simultaneous peaks in wind speed cause extreme amounts of melt energy, up to 722.3 W m^{-2}, resulting in continuous half-hourly melt rates of 3–4 mm w.e. Peaks in surface melt occur at 21:00 and 23:00 on February 6 as well as at 01:30 on February 7, aligning fairly well with coincident maxima in measured T_a, e_a and $LW\downarrow$ and modeled U and $PREC$. Accounting for 35% of melt energy, Q_{RAIN} is clearly the main energy source in this phase, while Q_L, Q_S and Q^*provide 30%, 25%, and 10% of Q_M, respectively. Comparatively high contributions of energy from rain (up to 37%) during large daily ablation have also been reported by Hay and Fitzharris (1988) for Ivory Glacier in the Southern Alps. Finally, at around 04:00 on February 7, post-event conditions are initiated by a sudden drop in T_a to less than 1°C and a sharp reduction of e_a and U (cf. Figure 3), resulting in strongly reduced turbulent heat fluxes and thus, surface melt. RH, $LW\downarrow$, and $PREC$ remain high until the end of the modeling period, pointing to residual (post-cold-frontal) cloud cover and rainy weather. The surface energy budget returns to normal summer ablation conditions with a clear dominance of radiative fluxes (48% of Q_M) but still high energy release from rain (23% of Q_M).

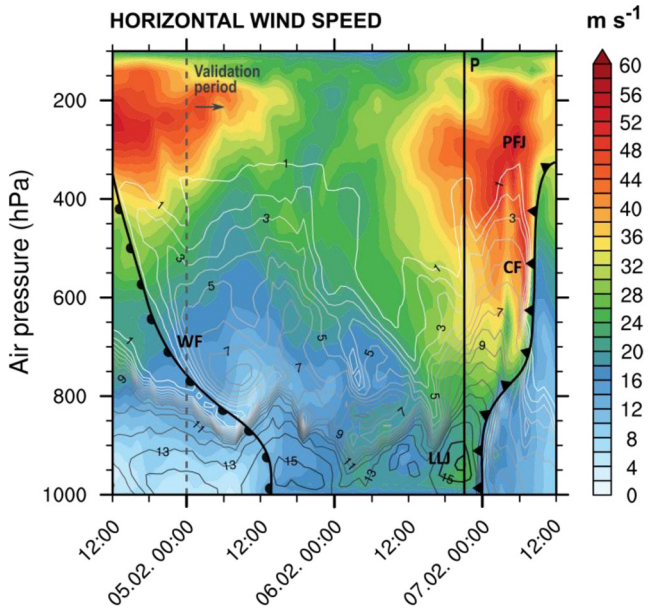

Figure 6. Temporal evolution of wind speed (shaded contours) and water vapor mixing ratio (g kg^{-1}; contour lines) upstream of the study site (box 1 in Figure 2b), with the estimated location of the LLJ, polar front jet (PFJ) and the passing warm (WF) and cold fronts (CF) marked. The position of the sample vertical profile (P) analyzed in Figure 7 is indicated by the black vertical lines.

3.4. Meso-Scale Processes

3.4.1. Background Flow Characteristics

The atmosphere's response to orography when an airstream strikes coastal mountains is largely governed by the thermodynamic and kinematic characteristics of the air upstream of coastal effects (background flow; cf. Figure 2b). The vertical distribution and evolution of wind speed and moisture throughout the case study (Figure 6) exemplify a typical cross-sectional profile of an extratropical cyclone, including: (1) a warm front sloping behind an upper-level jet core of the polar front jet, overlain by a stratiform cloud system that forms by the gradual synoptic ascent of the WCB upon the slanting frontal surface, (2) the succeeding warm sector with embedded LLJ that conveys warm air masses which are forced upwards in an area of deep convection ahead of (3) an approaching cold front, tied to the upper-level jet. Behind the convective updraft, the air masses ascend rearward upon the frontal slope, forming dense mid- and high-altitude stratiform clouds, while the lower levels successively dry out from the surface due to the intrusion of cold, post-frontal air (Bjerknes & Solberg, 1922; Houze, 1993).

Consistently, water vapor mixing ratio (q_v; Figure 6), IWV and *RH* (not shown) are strongly enhanced during the presence of the WCB (14:00 on February 5 to 00:00 on February 7) and exhibit two major peaks in the vicinity of the fronts, caused by the frontal (convective) ascents and associated vertical penetration of moisture. While the moisture peak behind the warm front develops gradually, is comparatively persistent and gains moisture from upper to lower levels (forward ascent of air), the moisture plume associated with the cold front evolves rapidly and moistens from lower to upper levels (convective updraft and steep rearward ascent of air). Evidence for an LLJ is given by a coincident peak in low-level (1,000–850 hPa) IWV (not shown), q_v, and *U* ahead of the cold front (Figure 6), displaced to the warm side of the corresponding 1,000–500 hPa IWV maximum (Ralph et al., 2004). To be defined as an LLJ, *U* is required to exhibit a maximum below 1.5 km that is at least 2 m s^{-1} larger than a local minimum aloft (Neiman et al., 2002) and usually reaches magnitudes of 20–30 m s^{-1} (e.g., Browning & Pardoe, 1973; Doyle, 1997; Katzfey, 1995; Ralph et al., 2017). Accordingly, we detect an LLJ core between 960 and 940 hPa with magnitudes up to 26 m s^{-1}. Below 850 hPa, the vertical wind profile shows a typical vertical shear characteristic of warm advection, i.e., clockwise turning of the wind with height (Figure 7; Ralph et al., 2005), with strong winds aloft that increase from mid to upper levels. The wind strengthens throughout the event, and a global maximum of *U* of almost 60 m s^{-1} develops at 300 hPa around 05:00 on February 7, indicating the passage of the upper-level jet stream. Similar velocities were found in upper-level jet cores of extratropical cyclones in New Zealand and other midlatitude regions (Browning & Pardoe, 1973; Katzfey, 1995; Neiman et al., 2008; Rauber et al., 2020).

The strong front-parallel wind speeds within the LLJ facilitate the effective and persistent advection of temperature and moisture from likely both local and subtropical source regions (Rauber et al., 2020) across the midlatitudes within a narrow band that results in an AR. Associated vertical humidity profiles (Figure 7) showing largely saturated conditions and high water vapor content (13–16 g kg^{-1}) between the surface and 900–850 hPa are consistent with AR soundings from the eastern Pacific Ocean near the Californian coast (Neiman et al., 2008; Ralph et al. 2004, 2005) and the Southern Ocean near Tasmania (Rauber et al., 2020). Neiman et al. (2011) and Ralph et al. (2004, 2017) reported average core IWV magnitudes of 1.9 cm (2.8 cm) between the surface and 800 hPa (500 hPa) for midlatitude ARs, while we observe 20%–25% smaller values of 1.5 cm (2.1 cm). This might be due to a weaker AR in our case, or due the fact that the core zone of the AR studied here encounters the New Zealand coast further south and is already depleted in moisture when it reaches the study region. Collectively, the observed conditions and vertical profiles of moisture and wind speed in the AR (Figure 7) match the commonly accepted description of the typical structure of ARs with

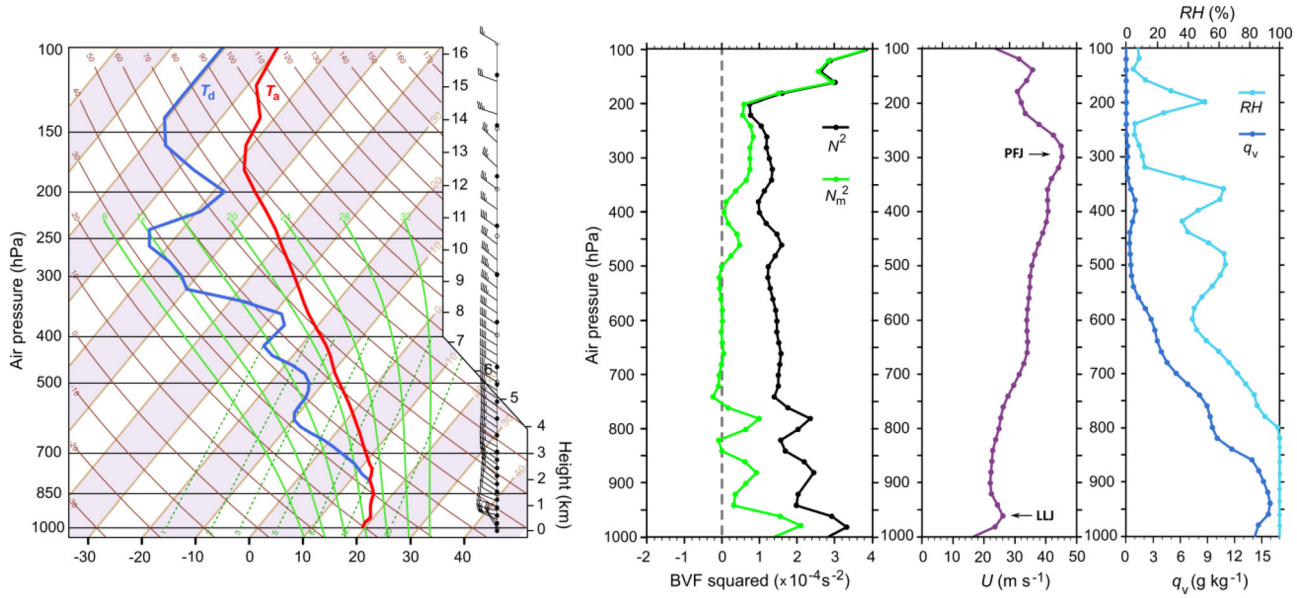

Figure 7. Thermodynamic characteristics of the upstream flow in the core zone of the AR at 21:00 on February 6, 2011, indicated by a Skew *T*-log*p* diagram as well as vertical profiles of the squared dry and saturated Brunt-Väisälä-Frequencies, wind speed, water vapor mixing ratio and relative humidity.

their association to upper- and lower-level jets as well as vertical frontal circulations and convection (Gimeno et al., 2014).

Due to the warm and moist nature of the air masses within the AR, its passage coincides with the intrusion of enhanced equivalent potential temperature. Although the dry static stability (N^2) indicates absolutely stable conditions throughout, saturated N_m^2 profiles and Skew *T*-log*p* diagrams reveal a more complex pattern of the atmospheric state, highlighting the prominent effect of high moisture content and largely saturated conditions near the surface on atmospheric stability. Throughout the case study, the saturated BVF suggests that the atmosphere is weakly stable to near moist neutral in case of full saturation, which might be reached near the mountain range; Skew *T*-log*p* diagrams indicate various sublayers of weak potential instability below 600 hPa that become more pronounced as the airflow gains moisture in the vicinity of the mountains (not shown). In the AR core zone, at 21:00–23:00 on February 6, both vertical profiles of N_m^2 and corresponding Skew *T*-log*p* diagrams indicate predominantly stable lower levels (1,000–750 hPa) and moist neutral conditions aloft up to 400 hPa (Figure 7). This reflects the typical stratification found in ARs and LLJs elsewhere (Browning & Pardoe, 1973; Neiman et al., 2011, 2008; Ralph et al., 2005). After the AR withdrawal and surface cold front passage (00:00 on February 7), thermodynamic profiles indicate a clear shift in the large-scale flow regime and air mass characteristics toward cold, moist but predominantly statically stable post-cold-frontal conditions (not shown).

To determine the behavior of the airflow when impinging on the Southern Alps, the interplay between wind speed, air mass stability and barrier height, as denoted by the Froude Number (*Fr*), is crucial. Values of $Fr < 1$ characterize a subcritical flow regime in which low-level flow is predominantly blocked (Doyle & Bond, 2001; Smith, 1979). Blocking may result in upstream flow deceleration and complex, non-linear mesoscale responses in the coastal zone, including stagnation, reversal, lateral deflection and splitting of the onshore flow, whereby a common response is the formation of a coast-parallel barrier jet (Overland & Bond, 1995; Pierrehumbert & Wyman, 1985). In a supercritical flow regime with $Fr >> 1$, the incident airflow can readily ascend and descend the mountain range by orographic lifting, which is often accompanied by the generation of linear flow features such as mountain waves (Doyle & Bond, 2001; Smith, 1979). $Fr \sim 1$ indicates a critical (or transitional) flow regime that is prone to exhibiting an internal hydraulic jump between sub- and supercritical regimes from one location or time to another. This regime has often been observed to occur in moist neutral flow conditions (Miglietta & Buzzi, 2001; Miglietta & Rotunno, 2005) and can lead to a complex pattern of cross-mountain flow and associated turbulent flow features such as wave breaking and downslope windstorms (Durran, 1990; Klemp & Lilly, 1975). The *Fr* of the bulk low-level

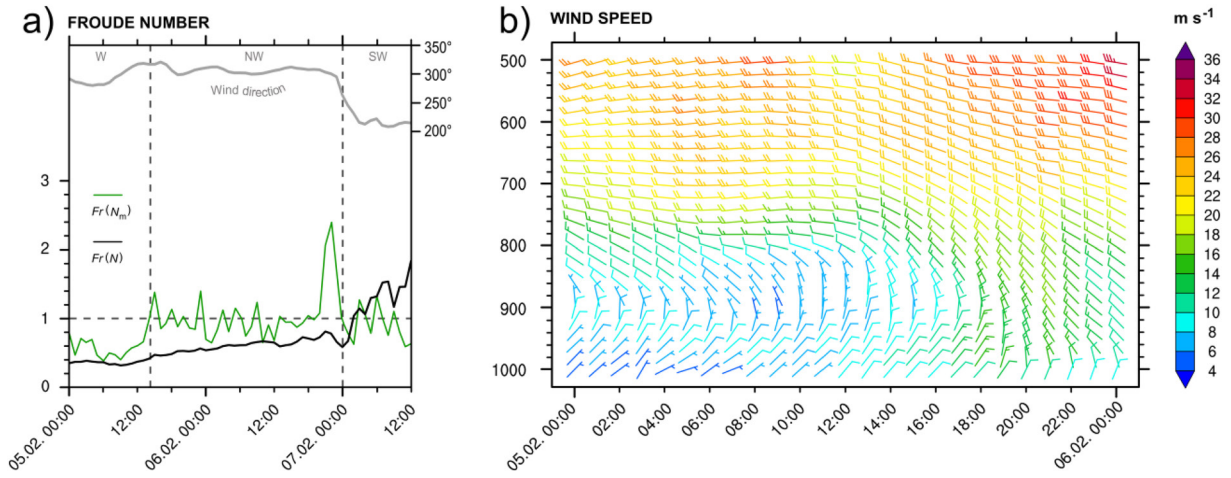

Figure 8. (a) Temporal evolution of wind direction and the dry and saturated Froude Numbers of the upstream (box 1 in Figure 2b) bulk low-level (1,000–800 hPa) flow, with the timing of the coincident switching in wind direction and flow regime ($Fr = 1$) emphasized by the dashed lines. (b) Temporal evolution of wind speed and direction throughout the atmospheric column, averaged over a region at the coast immediately offshore of Brewster Glacier (box 2 in Figure 2b). The wind barbs indicate a transition from initial low-level blocking and barrier jet formation to north-westerly overflow in the early phase of the case study.

upstream flow beneath ridge height (1,000–800 hPa) calculated from saturated N_m, which is considered more realistic than $Fr(N)$ due to the lower troposphere being largely saturated, shows that the effects of moisture enable the flow to largely overcome the barrier from around 14:00 on February 5 onwards (Figure 8a). This transition is coincident with the passage of the surface warm front and the arrival of the WCB, indicated by wind direction turning from W to NW (Figure 8a). Weak static stability, high wind speeds and associated large kinetic energy within the north-westerly warm-sector airflow thus suggest a transition from a non-linear "blocked" to a linear "flow-over" or at least critical regime at 14:00. The subsequent oscillatory behavior of Fr, characterized by fluctuations within a narrow range around 1, is likely caused by variations in low-level moisture content and suggests that there might be the potential of the air mass to undergo partial blocking and hydraulic switching associated with non-linear flow dynamics throughout the case study. The passage of the AR is marked by a distinct spike in Fr around 21:00 on February 6, pointing to a predominant direct overflow of the Southern Alps due to the high moisture and wind speed in the AR. A sudden shift in wind direction to the south-west at 00:00 on February 7 finally indicates the passage of the surface cold front (Figure 8a). Overall, the virtual absence of blocking combined with the moist-neutral (and partially moist-unstable) stratification in the warm sector flow give rise to the presumption that coastal mountains oriented normal to the 306° mean orientation of the low-level flow in the WCB and AR should be favored regions for large amounts of rainfall due to orographic enhancement (Neiman et al., 2002, 2011).

3.4.2. Flow Encountering the Southern Alps

Wind-vector maps (Figure 9) and vertical cross profiles (Figure 10) simulated in D2 confirm the flow behavior inferred from Fr of the upwind flow. The initial blocking of the incident pre-warm-frontal low-level (1,000–800 hPa) airflow leads to large-scale flow stagnation and flow splitting upstream of the mountain barrier. Instead of diverting either side of the mountain, only a small portion of the flow is deflected to the left (north-east to east) and passes through Cook Straight, while the vast majority is diverted to the right (south) due to the Southern Hemisphere Coriolis force decreasing in response to the flow deceleration (McCauley & Sturman, 1999; Pierrehumbert & Wyman, 1985). The diverted flow accelerates down the along-barrier pressure gradient, leading to the formation of a ridge-parallel, north-easterly barrier jet (Figure 9, T1). The jet is marked by a characteristic strong directional shear from north-westerly flow above the barrier height to north-easterly (~62°) winds below 900 hPa, and features a core of maximum wind velocity at 960–940 hPa (450–650 m) that reaches 9–16 m s^{-1} in the coastal region offshore of Brewster Glacier (Figure 8b). Near the south-western tip of the South Island the jet speeds up to >30 m s^{-1} when merging with the airstream passing the country to the south through Foveaux Strait. The jet emerges rapidly at around 18:00 on February 4 and reaches its maximum lateral extent of >200 km (Figure 9, T1) within only a few

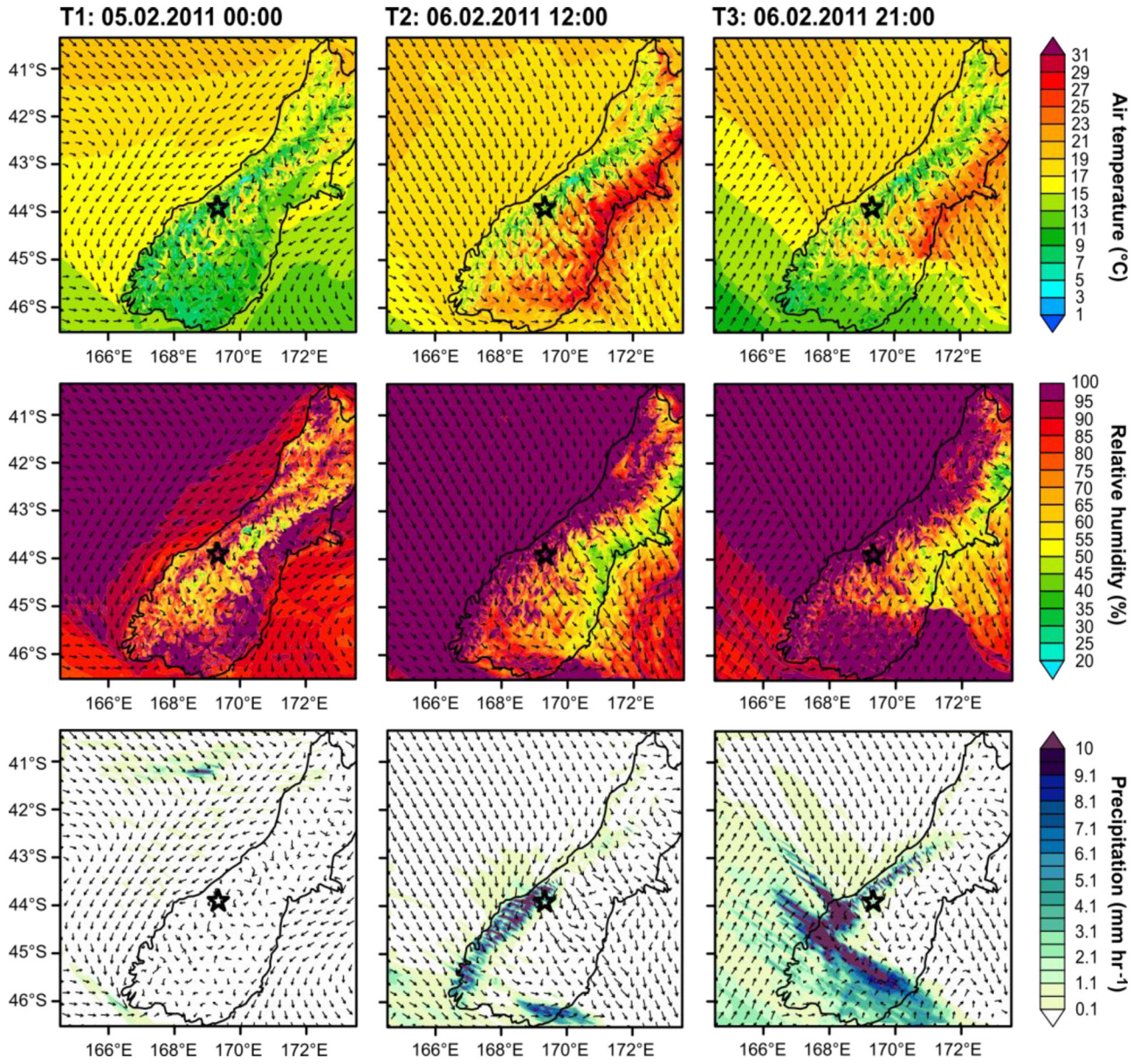

Figure 9. Spatial distribution of surface air temperature, relative humidity and precipitation across D2 for different time snapshots during the case study, demonstrating the presence of a barrier jet (T1), foehn effect (T2) and impingement of the AR core zone ahead of the approaching cold front (T3). All variables except precipitation (surface variable) were taken from the lowest model level (~9 m above ground), with vectors indicating the corresponding wind direction.

hours, while its coastal core strengthens more gradually. This is similar to findings from Revell et al. (2002) who described a situation of blocked flow at the west coast of the South Island that involved an abrupt deceleration of the flow field to more than 250 km upstream of the coast and the progressive evolution of a barrier jet with at least 120 km lateral extent. The approaching warm front and WCB successively supersede the barrier jet by causing low-level air to become increasingly involved in orographic uplift (transition to "flow-over" regime). In total, the jet persists for ~24 h until 18:00 on February 5 (Figure 8b), coincident with the start of precipitation and increasing surface energy fluxes on Brewster Glacier that lead to the onset of the melt event (cf. Figure 5; PH 1). It would be of interest for a future study to compare the modeling results to additional data such as observed wind products, which we presently do not have access to; however, overall, the properties (direction, magnitude, depth, extent, persistence) of the simulated barrier jet do compare notably well to those reported from other studies concerned with barrier jets along the south-western New

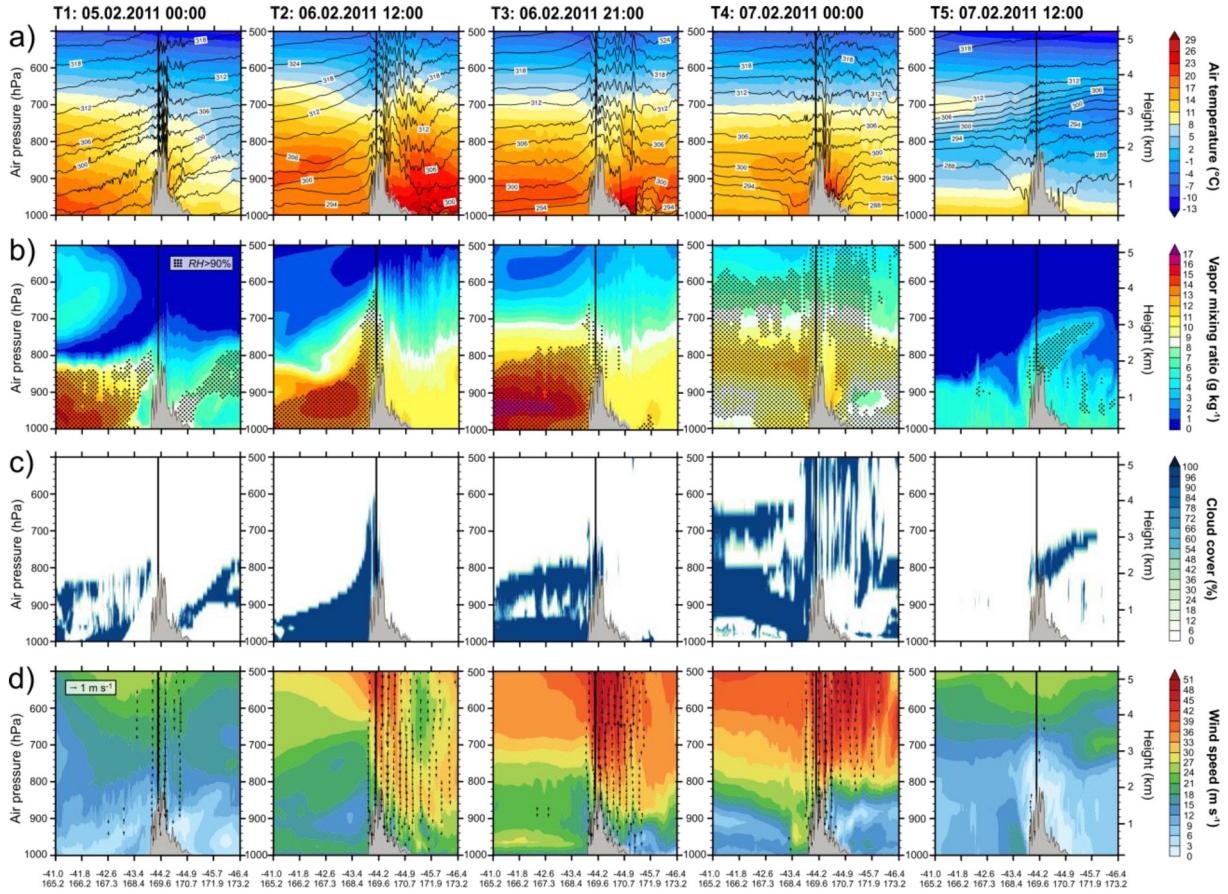

Figure 10. Vertical cross profiles capturing the most distinct stages of airflow modification when the upstream flow encounters the Southern Alps. The snapshots represent: Pre-warm-frontal conditions with orographic blocking (T1); overflow and foehn development during warm sector flow (T2) and during flow within the core zone of the AR (T3); time of the cold front passage associated with spill-over (T4); post-cold-frontal conditions (T5). The filled gray areas in each plot delineate the land surface, with the vertical black line marking the location of Brewster Glacier. Contour lines in (a) represent potential temperature, stippling in (b) highlights regions with $RH > 90\%$, and vectors in (d) show the vertical wind component (direction and magnitude), with the reference vector given in the leftmost plot.

Zealand coast (McCauley & Sturman, 1999; McGowan & Sturman, 1996; Revell et al., 2002). The occurrence of orographic blocking and barrier jet development is a common phenomenon in New Zealand and has occurred in association with many mountain ranges worldwide including the Andes (Temme et al., 2020), the European Alps (Bousquet & Smull, 2003), Antarctica (Schwerdtfeger, 1975), the Sierra Nevada (Parish, 1982), and Taiwan (Yeh & Chen, 2003). Some of these events have been associated with the landfall of LLJs and ARs (Bozkurt et al., 2018; Neiman et al. 2002; Viale et al., 2013).

A common observation with blocked flow is an upwind redistribution of precipitation, with amounts enhanced upstream of the coast and reduced over the mountain slopes. This feature is due to barrier jets often being capped by a layer of enhanced static stability, which acts as a local baroclinic zone inducing mechanical uplift of the approaching air masses before they actually reach the topography (Bousquet & Smull, 2003; Doyle, 1997; Neiman et al., 2002; Sauter, 2020; Sinclair et al., 1997). An upwind concentration of precipitation is clearly evident during the early phase of the case study (Figure 9, T1), where precipitation is restricted to the offshore zone and maximum rain rates occur at the upstream edge of the barrier jet. Further note the inclined potential temperature- (θ-) isentropes and the sloping isolines of moisture (q_v and RH) and cloud cover in the vertical cross sections of Figure 10.

Mountain overflow of the weak moist-stable to moist-neutral warm-sector air promotes the formation of gravity waves that propagate vertically from over the Main Divide into the lee (eastern) side of the Southern Alps, evident by the distortion of the θ- and vertical wind fields (Figure 10a and 10d). While the waves are

comparatively weak during initial blocking, wave amplitudes thereafter increase substantially, allowing the upwind air to penetrate deep into the leeside surface layer. This is likely favored by the frequent periods with $Fr \sim 1$ (Figure 8a), characterizing a critical flow regime in which the airflow is prompted to undergo spontaneous transitions between non-linear and linear states, which is typically conducive to large-amplitude waves and non-linear flow features such as wave overturning. These often ensue strong downslope windstorms at the lee slopes (Figure 10d) which are succeeded by an abrupt readjustment to ambient, subcritical conditions further downwind in the form of a hydraulic jump (Elvidge et al., 2014; Miglietta & Rotunno, 2005). Mountain waves and distortions of the θ- and wind fields are characteristic phenomena during foehn events (King et al., 2017; Turton et al., 2017), which are classically defined as warm, dry winds descending in the lee of a mountain range, causing substantial increases (decreases) in leeside temperature (humidity) relative to the windward side of the ridge (Brinkmann, 1971).

Indications of foehn development provided by the orographic modification of the flow pattern are supported by the cross-barrier change in air mass characteristics. Both vertical fields and surface maps of T_a, q_v and RH demonstrate the continuous pile-up of the warm and moist low-level air masses within the WCB and AR (since 18:00 on February 5) at the windward slopes of the Southern Alps, resulting in intense cloud cover and orographic precipitation development within this "foehn wall" (Figures 9 and 10a–10c; T2–T3). Until 21:00 on February 6, when the AR core reaches the coast offshore of Brewster Glacier, the Main Divide represents a sharp demarcation, to the east side of which RH and q_v are significantly reduced and cloud cover is zero ("foehn clearance"; Hoinka, 1985). In addition to the sharp depletion in moisture, conditions at the leeside are marked by a pronounced low-level warming as indicated by the strong increase of T_a in the eastern valleys and foothills that reaches far down to the east coast of the South Island (Figures 9 and 10a). The combined effect of decreasing humidity, increasing air temperature and locally enhanced surface wind speeds (Figure 10d) in the mountain leeside persists during nighttime and is characteristic of a foehn effect with associated cross-barrier warming and drying and severe downslope winds in lee valleys (Durran, 1990; Klemp & Lilly, 1975; McGowan et al., 1996). For example, comparison of near-surface humidity, temperature and horizontal wind speed at two sites along the cross-section, located at comparable altitudes (~870 m) immediately west and east (near Omarama) of the Southern Alps, respectively, revealed a marked drop in RH from 100% to 50%, a reduction of q_v by ~1 g kg^{-1}, an increase of T_a by almost 8 K and strong local wind speeds up to 15 m s^{-1}. These values agree well with cross-topography gradients measured during foehn conditions elsewhere (e.g., Bannister & King, 2015; Elvidge et al., 2014; Richner et al., 2006). Maps of surface meteorological conditions (Figure 9) further suggest that the "foehn anomaly" (Elvidge et al., 2014) is most significant where the barrier is highest, that is, in the area of Mount Cook (3,724 m), and reveal that horizontal wind speeds can reach up to 40 m s^{-1} on the lee slopes and within the major inlets and river valleys, such as around at Lake Tasman and Pukaki (not shown). Foehn in the Southern Alps of New Zealand, locally termed the *nor'wester*, is very common, with several events (some involving wind speeds up to 50–60 m s^{-1}) being well documented in literature (e.g., McGowan & Sturman, 1996; McGowan et al., 1996, 2002). In addition, foehn winds that develop in response to the impingement of an AR onto a topographic barrier have recently been detected in Antarctica (Bozkurt et al., 2018; Wille et al., 2019) and exhibit very similar synoptic and mesoscale features as those presented here.

The foehn effect abates in the eastern foothills from 20:00 onwards on February 6 due to the successive intrusion of cold south-westerly air, and it finally ceases around 00:00 on February 7, coincident with the passage of the cold front and associated synoptic mid- to upper-level clouds. These cause a rapid dispersion of the cross-barrier temperature and humidity gradient by promoting heavy precipitation (Figure 9, T3) and a progressive spill-over of moisture to the east of the Main Divide (Figures 10b–10c, T3–T4). Spill-over of moisture and precipitation into the mountain leeside is reported from other New Zealand studies (Chater & Sturman, 1998; Sinclair et al., 1997), where it was related to the passage of active fronts over the Southern Alps, such as during the final stages of foehn effects (McGowan & Sturman, 1996). From 00:00 on February 7 onwards, the lower levels become entrained by cold, post-frontal south-westerly air to either side of the ridge, while mid- and upper-level clouds and associated precipitation and spill-over persist until ~08:00 on February 7. After the full dispersal of the high cloud, a banner cloud remains anchored to the mountain crest, which most likely forms by the leeside ascent and vortex formation of the highly non-linear post-frontal flow (Figures 10b–10c, T5).

There are different theories of foehn wind development and various explanations for its association with leeside warming and drying (Elvidge & Renfrew, 2016; Elvidge et al., 2014). We propose that the observed foehn is mainly thermodynamically induced, by the irreversible latent heating of the upstream air due to ascent, condensation and precipitation development over the windward slopes (thermodynamic mechanism). Strong mountain wave activity and severe downslope winds experienced at the leeside helped to effectively draw this warmed air into the leeside surface layer under additional dry adiabatic warming. The foehn was, however, at least initiated by the isentropic advection of potentially warmer higher level air down the lee slopes (isentropic drawdown mechanism), given the initial orographic blocking and barrier jet presence. The arrival of the WCB at 14:00 on February 5 did therefore not only cause a change in flow regime from a non-linear (subcritical or partially blocked) to a largely linear (supercritical or "flow-over") or at least critical regime but also likely promoted the transition between foehn mechanisms (Elvidge et al., 2014; King et al., 2017). Leeside mechanical turbulent mixing and radiative warming due to the dry, clear-sky foehn conditions (Elvidge & Renfrew, 2016) may have also contributed to leeside warming and drying. It is, however, beyond the scope of this study to determine the exact cause of the foehn effect, especially because it does not influence the mass of Brewster Glacier directly due to its location on the windward side of the mountain and at high elevation. Leeside foehn conditions may, however, be highly important for glaciers situated at the eastern side of the Main Divide.

3.4.3. Atmospheric Dynamics Above Brewster Glacier

The mesoscale modulation of the airflow by the mountains determines the state of the ABL above Brewster Glacier, which in turn governs the conditions and processes at the glacier surface. Since turbulent heat fluxes and the heat released from liquid precipitation have been identified as crucial drivers of high glacial ablation during the case study, we focus particularly on the mechanisms of cloud and precipitation development, as well as their composition and phase.

While during pre-event conditions (prior to 18:00 on February 5; cf. Figure 5), when the upstream flow is blocked, both cloud fraction and the concentration of cloud condensates (<0.1 g kg^{-1}) in the Brewster region are low, the event itself (between 18:00 on February 5 and 04:00 on February 7) is characterized by an overall dense cloud cover and high condensate mixing ratios (q_c; Figure 11a). In the first stage of this time window, until about 21:00 on February 6, clouds are confined to low- and mid-levels (900–700 hPa), with the cloud top varying between 750 and 550 hPa and the core zone (area of maximum total q_c) being located at around 850–800 hPa, coincident with the approximate height of the mountain crest. According to the Morrison 2-moment microphysics scheme used in the modeling, these low- to mid-level clouds consist more or less of equal shares of rain and cloud water at the level of Brewster Glacier (Figure 11a), with high amounts of rainwater coinciding with peaks in modeled precipitation (cf. Figure 3). As the clouds near the ground are largely saturated ($RH \sim 100\%$) and water vapor pressure exceeds the saturation pressure over ice of 6.11 hPa (cf. Figure 3), glacial melt is promoted by an intensification of the turbulent latent heat flux toward the glacier surface. Furthermore, especially during PH2, when cloud thickness and cloud water ratios are high, strong condensation rates within the low-level clouds are likely to additionally enhance melting by releasing large amounts of latent energy, which may indirectly increase the surface sensible heat flux (by increasing the temperature of the air mass) and/or the rain heat flux (by promoting rainfall) at the glacier surface.

The clouds during PH1 and PH2 are assumed to be a combination of pre-existing synoptic clouds and orographically induced clouds that form due to windward mechanical lifting and condensation of the moist low- to mid-tropospheric warm-sector air masses, and accumulate within the foehn wall near the Main Divide where Brewster Glacier is located. They are largely stratiform ($N_m^2 > 0$), with a distinct convective region ($N_m^2 < 0$) located at 750–600 hPa. This region becomes particularly prominent between 09:00 and 21:00 on February 6 (PH2), with almost 50% of the cloudy grid cells being unstable (Figure 11b). The observed pattern appears plausible as both observational (Browning et al., 1974; Houze & Medina, 2005; Medina & Houze, 2003; Rotunno & Houze, 2007) and idealized modeling studies (Fuhrer & Schär, 2005; Kirshbaum & Durran, 2004; Smith, 1979) have shown that orographic uplift of moist, neutral to marginally unstable air typically produces nominally stratiform orographic clouds on the windward side of a mountain range, which can feature embedded, closely packed convective cells formed by shallow convection. As revealed by background flow analysis, the upstream air masses are characterized by regions of conditional instability,

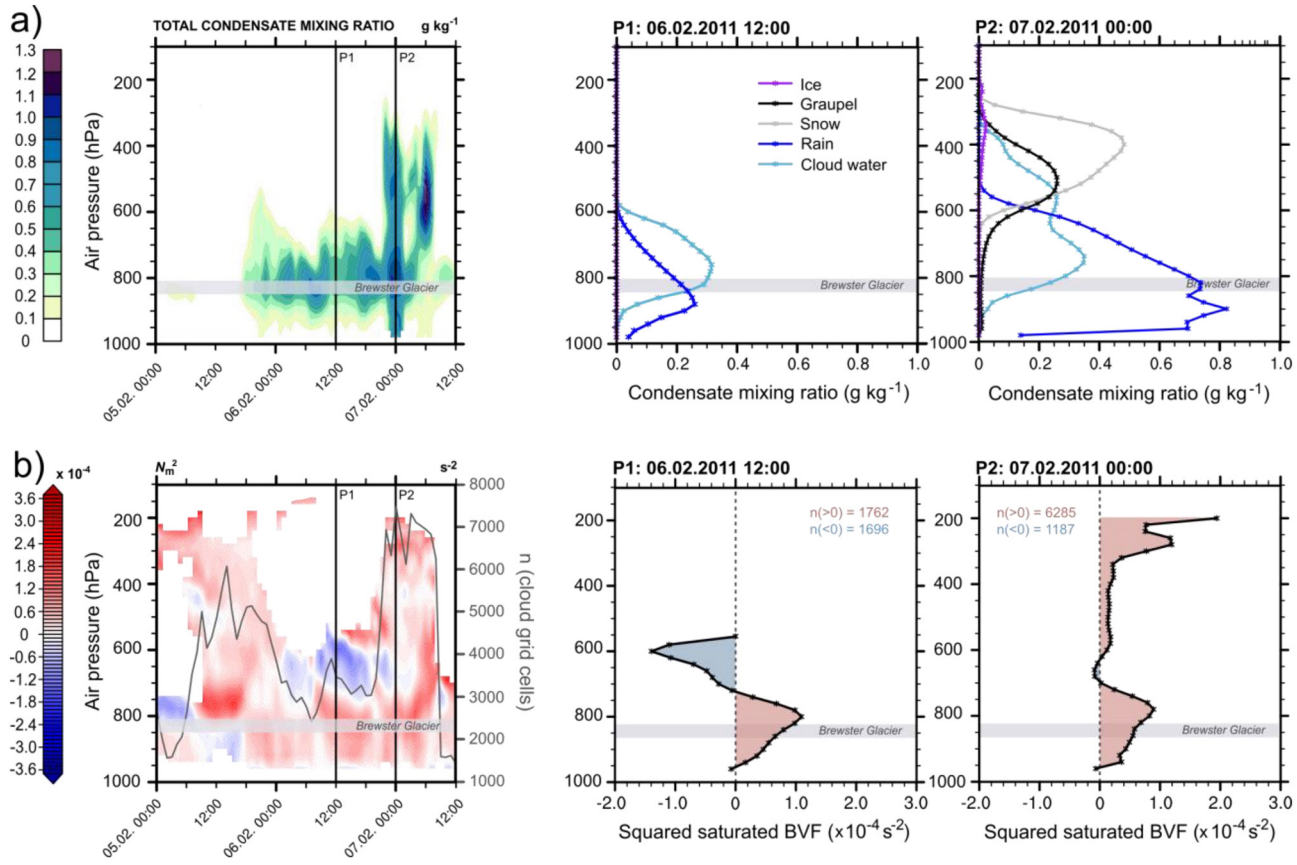

Figure 11. Temporal evolution of clouds (structure and composition) above Brewster Glacier (box 3 in Figure 2b), indicated by (a) the vertical distribution of the total condensate mixing ratio and (b) the squared saturated Brunt-Väisälä-Frequency of cloudy grid cells, defined as the number of grid cells per time step, which exhibit a total condensate mixing ratio > 0 (indicated by the gray line referring to the right y-axis). Vertical black (P1 and P2) lines in (a) and (b) mark time snapshots, for which the vertical distribution of hydrometeors and N_m^2, respectively, are depicted in the corresponding panels on the right side. Numbers in (b) give the number of grid cells with $N_m^2 > 0$ (static stability) or $N_m^2 < 0$ (static instability).

thus holding the potential to trigger cellular convection within the otherwise stratiform orographic cloud system. The existence of embedded convective motion within clouds can lead to significantly increased precipitation amounts, intensity and efficiency compared to a uniformly stable cloud system, since the cellular overturning produces pockets of increased cloud liquid water content, where invigorated microphysical processes quickly convert condensate to precipitation-sized particles (Fuhrer & Schär, 2005; Houze & Medina, 2005; Kirshbaum & Durran, 2004). This may be one explanation for the strong turbulent heat fluxes and the extreme amounts of rainfall experienced on Brewster Glacier during the case study.

At 21:00 on February 6 (PH3), a dense, high-reaching cloud column emerges in the model simulation, that extends to over 300 hPa and persists until about 08:00 on February 7 (Figure 11a). It represents the high synoptic cloud (presumably cumulonimbus-type) associated with the passing cold front. The cloud is predominantly stable with scattered embedded convective regions (Figure 11b) and is composed of ice (400–200 hPa), snow and graupel (700–300 hPa) at mid to upper levels and rain at lower levels (≥600 hPa), with cloud water occurring throughout. Graupel peaks at a lower height than snow, extending down to approximately 800 hPa (Figure 11a).

The simulated vertical distributions of hydrometeors (Figure 11a) and cloud fraction (not shown) further suggest that there are two centers of microphysical activity within the cloud, one at 850–750 hPa and the other located at 550–450 hPa. This points to the presence of two separately operating but vertically connected cloud systems, namely, the constantly reproducing orographic cloud at lower levels and the intruding mid- to high-tropospheric frontal cumulonimbus cloud. The two precipitating systems are assumed to interact in the form of a seeder-feeder-mechanism (Bergeron, 1965) to enhance orographic precipitation and

produce the extreme amounts of rain (up to 32 mm h^{-1} in WRF) experienced at the glacier surface. The mechanism implies that cloud droplets and/or ice crystals from the synoptic seeder cloud aloft fall into the orographic feeder cloud, where collision and coalescence and/or accretion cause a rapid growth in precipitation particles and thus increase precipitation at the surface to volumes greater than would be possible by each cloud system individually (Purdy et al., 2005). This is supported by the modeling which indicates that during peak cloud cover, the share of rain in hydrometeors at lower levels (950–700 hPa) significantly increases compared to prior conditions where only the orographic cloud was present (Figure 11a). The occurrence of convective dynamics throughout the cloud column (Figure 11b) may additionally contribute to precipitation enhancement by both accelerating the formation of raindrops in the lower orographic cloud (see above) and by catalyzing ice particle collisions and aggregation as well as coalescence and riming in the upper frontal cloud system, thereby promoting the fallout of ice hydrometeor mass in the form of rimed aggregates or graupel (Houze & Medina, 2005). Support for this process is provided by the modeled large quantities of graupel occurring within the cloud system above Brewster Glacier (Figure 11a). A range of studies have recognized orographic enhancement of frontal precipitation due to either or both of the two named mechanisms (Browning et al., 1974; Carruthers & Choularton, 1983; Rotunno & Houze, 2007; Viale et al., 2013), including for New Zealand (Purdy & Austin, 2003; Purdy et al., 2005; Revell et al., 2002; Wratt et al., 2000). Furthermore, Finlon et al. (2020) found observational evidence for the seeder-feeder mechanism operating in an AR over the ocean south-east of Australia. In accordance with Wratt et al. (1996), we propose a combination of the seeder-feeder-mechanism and convective dynamics triggered by the release of conditional instability through uplift to be a potential driver of the large observed orographic rainfall enhancement and associated high ablation rates to the west of the Main Divide in the Southern Alps.

At 01:00 on February 7, cold and moist south-westerly post-frontal air progressively intrudes into the atmospheric column from lower to upper levels, leading to a gradual dispersion of the orographic cloud. At the elevation of Brewster Glacier (~820 hPa), clouds disperse around 04:00, thus initiating post-event conditions (cf. Figure 5). The upper ranges (<700 hPa) of the towering frontal cloud persist until about 07:00 and cause a late precipitation peak between 06:00 and 07:00 (cf. Figure 3). This rain shower is, however, less intense than the preceding ones since it is produced by the mid-level, predominantly snow-containing cloud alone. From 07:00 onwards, there is an overall cloud clearing.

4. Conclusions

In this study, we used a high-resolution atmospheric simulation with WRF to reveal the mesoscale processes governing a typical extreme ablation event on Brewster Glacier in the Southern Alps of New Zealand. This is the first time, to our knowledge, that a mesoscale atmospheric model is used to investigate mass balance responses to large-scale atmospheric dynamics on a New Zealand glacier. The case study focused on an extreme melt event that occurred on February 6, 2011 during the landfall of an AR on the south-western coast of the South Island.

SEB investigations revealed that the melt event was locally driven by high surface air temperatures, enhanced atmospheric humidity and heavy rainfall (133.4 mm w.e. d^{-1}). These resulted in strong turbulent (predominantly latent) and rain heat fluxes producing large amounts of melt energy, up to 722.3 W m^{-2}. On the synoptic scale, the AR occurred within north-westerly airflow and was induced by a LLJ residing in the lower atmosphere within the WCB ahead of a surface cold front that was tied to an approaching upper-level wave trough. Based on the hourly model data, we investigated the mechanisms that transformed the high temperature and water vapor of the approaching flow into enhanced rainfall, turbulent fluxes and thus, melt on Brewster Glacier. By partitioning the analysis into three components targeting (i) the background flow, (ii) the orographically modified flow, and (iii) the structure and dynamics of clouds and precipitation in the ABL above Brewster Glacier, the following processes were identified:

- The arrival of the warm conveyor belt behind a surface warm front that passed the study region prior to the event at 14:00 on February 5, 2011 caused a change in Froude Number and thus, a transition from an initially blocked ($Fr \ll 1$) to a "flow-over" or at least critical flow regime ($Fr \geq 1$). This enabled the warm, low-shear and moist-neutral to marginally unstable upstream air masses within the warm sector flow and AR to ascend the mountains.

- The change in flow regime led to the cessation of the earlier established, coast-parallel, north-easterly barrier jet, and to a shift of clouds and precipitation from the upstream edge of the blocked flow to over the western (windward) slopes of the Southern Alps. As the air mass continued to pass over the mountain range to the leeside, a gravity wave developed, and a thermodynamic foehn effect was created, which caused warm and dry conditions as well as cloud dissipation ("foehn clearance") and strong downslope winds at the mountain leeside. Brewster Glacier was situated just within the high-condensation environment of the orographic cloud immediately west of the Main Divide.
- Windward precipitation was orographically enhanced by the development of convective cells in the orographic cloud, resulting from the release of potential instabilities within the upstream flow through mechanical lifting and orographically forced updraft. Very large amounts of rain occurred during the combined passage of the AR and cold front at 00:00 on February 7, 2011 as this most likely led to an effective combination of precipitation from lower- and mid- to upper-level precipitating systems by the seeder-feeder-mechanism.

These findings prompt the conclusion that, on the local scale, melt on Brewster Glacier was strongly enhanced due to: (i) high sensible and latent heat fluxes caused by moderate wind speeds combined with high temperatures and moisture content, respectively, of the impinging warm-sector and AR air masses; the high turbulent latent heat flux to the glacier surface is thereby assumed to have been particularly favored by the low-level orographic cloud; (ii) increased incoming longwave radiation due to the mentioned high cloud cover amount, and (iii) exceptionally large energy inputs from liquid precipitation falling on the glacier surface, partly originating from convective cloud regions and from the wash-out of the orographic cloud by rain droplets from a synoptic seeder cloud aloft.

The vertical distribution of hydrometeors (cf. Figure 11) during this summertime case study suggests that Brewster Glacier was situated only slightly below a critical altitude near the freezing point where the occurrence of various hydrometeor types and thus precipitation phases is very likely. This highlights the importance of seasonality for its mass balance, as discerned in previous studies (e.g., Little et al., 2019). Since similar large-scale forcing mechanisms, that is, north-westerly airflow with embedded ARs, have been found to control both extreme ablation and accumulation in summer and winter, respectively, air temperature seems a key for the impact on glacier mass balance by dictating whether an extreme event will result in rain or snowfall and thus mass loss or mass gain at the glacier surface (Anderson & Mackintosh, 2012; Little et al., 2019).

While the processes promoting high melt on Brewster Glacier during the event might apply to other glaciers on the windward side of the Main Divide, glaciers situated further to the east, outside of the foehn wall, could, conversely, be affected by leeside foehn conditions, that is, high shortwave radiation due to foehn clearance and increased sensible heat flux from strong downslope winds. These effects would also be evident during upwind blocking conditions, when the formation of an along-ridge barrier jet can shift orographic precipitation from the mountain slopes further upstream. There might thus be a different response of glaciers situated at the western and eastern sides of the Main Divide during the same large-scale conditions, as recognized earlier by Purdie et al. (2011) for Franz Joseph and Tasman glaciers and found for other foehn-affected glacier environments as well (e.g., Temme et al., 2020).

We note that there are some uncertainties in our results given the limited study period and the potential sensitivity to model settings including the choice of the microphysics parameterization. However, the model's ability to reproduce local meteorological conditions (cf. Section 3.1) lends confidence to the key processes identified in our analysis. Furthermore, the case study showed that the consideration of mesoscale processes alongside micro- and large-scale observations enabled us to draw a consistent, multi-scale picture of the mechanisms triggering high melt on a glacier in the Southern Alps and lends support to the hypothesis that mesoscale processes represent an integral element of the glacier-climate relationship in the Southern Alps. The case study thus demonstrated the possibility of how to advance understanding of glacier-atmosphere links in the Southern Alps of New Zealand, underlining the benefit of mesoscale atmospheric modeling in this research field. For future studies, it would be worthwhile to couple the WRF model with a SEB model and perform sensitive experiments to explicitly evaluate the role of different mechanisms on orographic precipitation, and on the surface energy and mass fluxes at the glacier surface. This would also enable a more precise assessment of how the future development of air temperature and changes in the frequency

and occurrence of extratropical cyclones and ARs in the New Zealand region will impact the evolution of Southern Alps glaciers, as windward orographic precipitation, leeside foehn effects and spill-over depend on such dynamics.

Data Availability Statement

Data supporting the research study are included in an open access data base at https://doi.org/10.5281/zenodo.4252462. Other employed data sets (see Section 2) are freely available from the National Aeronautics and Space Agency (NASA; Jarvis et al., 2008), European Centre for Medium-Range Weather Forecasts (ECMWF; Hersbach et al., 2020), and Randolph Glacier Inventory (RGI; Pfeffer et al., 2014) platforms. Synoptic charts (see Section 2.4) are not publically accessible but are provided on request by MetService New Zealand; meteorological records and surface energy and mass balance data (see Section 2.2) are described in Conway and Cullen (2016) and Cullen and Conway (2015).

Acknowledgments
This work was supported by the Alexander von Humboldt Foundation and the German Research Foundation grant MO 2869/4-1. The authors gratefully acknowledge the compute resources and support provided by the Erlangen Regional Computing Center (RRZE) whilst running the WRF model. The authors want to thank Jono Conway for providing energy and mass balance data as well as information about surface conditions on Brewster Glacier. The authors further acknowledge the constructive comments from the three reviewers, which improved and clarified the manuscript, and Dr. L. Ruby Leung for editing. Open access funding enabled and organized by Projekt DEAL.

References

Albergel, C., Dutra, E., Munier, S., Calvet, J.-C., Munoz-Sabater, J., de Rosnay, P., & Balsamo, G. (2018). ERA-5 and ERA-Interim driven ISBA land surface model simulations: Which one performs better? *Hydrology and Earth System Sciences*, *22*(6), 3515–3532. https://doi.org/10.5194/hess-22-3515-2018

Anderson, B., & Mackintosh, A. (2012). Controls on mass balance sensitivity of maritime glaciers in the Southern Alps, New Zealand: The role of debris cover. *Journal of Geophysical Research*, *117*(F1), F01003. https://doi.org/10.1029/2011JF002064

Andreas, E. L., Claffey, K. J., Jordan, R. E., Fairall, C. W., Guest, P. S., Persson, P. O. G., & Grachev, A. A. (2006). Evaluations of the von Kármán constant in the atmospheric surface layer. *Journal of Fluid Mechanics*, *559*, 117–149. https://doi.org/10.1017/S0022112006000164

Bannister, D., & King, J. (2015). Föhn winds on South Georgia and their impact on regional climate. *Weather*, *70*(11), 324–329. https://doi.org/10.1002/wea.2548

Bergeron, T. (1965). On the Low-Level Redistribution of Atmospheric Water Caused by Orography. In *Proceedings of the International Conference on Cloud Physics, May 24–June 1, 1965, Tokyo and Sapporo. Supplement* (pp. 96–100).

Bjerknes, J., & Solberg, H. (1922). Life cycle of cyclones and the polar front theory of atmospheric circulation. *Geophysisks Publikationer*, *3*(1), 3–18.

Bousquet, O., & Smull, B. F. (2003). Observations and impacts of upstream blocking during a widespread orographic precipitation event. *Quarterly Journal of the Royal Meteorological Society*, *129*(588), 391–409. https://doi.org/10.1256/qj.02.49

Bozkurt, D., Rondanelli, R., Marín, J. C., & Garreaud, R. (2018). Foehn event triggered by an atmospheric river underlies record-setting temperature along Continental Antarctica. *Journal of Geophysical Research: Atmospheres*, *123*(8), 3871–3892. https://doi.org/10.1002/2017JD027796

Braun, M. H., Malz, P., Sommer, C., Farías-Barahona, D., Sauter, T., Casassa, G., et. al. (2019). Constraining glacier elevation and mass changes in South America. *Nature Climate Change*, *9*, 130–136. https://doi.org/10.1038/s41558-018-0375-7

Brinkmann, W. A. R. (1971). What is a foehn? *Weather*, *26*(6), 230–240. https://doi.org/10.1002/j.1477-8696.1971.tb04200.x

Browning, K. A., Hill, F. F., & Pardoe, C. W. (1974). Structure and mechanism of precipitation and the effect of orography in a wintertime warm sector. *Quarterly Journal of the Royal Meteorological Society*, *100*(425), 309–330. https://doi.org/10.1002/qj.49710042505

Browning, K. A., & Pardoe, C. W. (1973). Structure of low-level jet streams ahead of mid-latitude cold fronts. *Quarterly Journal of the Royal Meteorological Society*, *99*(422), 619–638. https://doi.org/10.1002/qj.49709942204

Carruthers, D., & Choularton, T. (1983). A model of the feeder-seeder mechanism of orographic rain including stratification and wind-drift effects. *Quarterly Journal of the Royal Meteorological Society*, *109*(461), 575–588. https://doi.org/10.1002/qj.49710946109

Chater, A. M., & Sturman, A. P. (1998). Atmospheric conditions influencing the spillover of rainfall to lee of the Southern Alps, New Zealand. *International Journal of Climatology*, *18*(1), 77–92. https://doi.org/10.1002/(sici)1097-0088(199801)18:1<77::aid-joc218>3.0.co;2-m

Chinn, T., Fitzharris, B. B., Willsman, A., & Salinger, M. J. (2012). Annual ice volume changes 1976–2008 for the New Zealand Southern Alps. *Global and Planetary Change*, *92–93*, 105–118. https://doi.org/10.1016/j.gloplacha.2012.04.002

Chinn, T. J., Heydenrych, C., & Salinger, M. J. (2005). Use of the ELA as a practical method of monitoring glacier response to climate in New Zealand's Southern Alps. *Journal of Glaciology*, *51*(172), 85–95. https://doi.org/10.3189/172756505781829593

Clare, G. R., Fitzharris, B. B., Chinn, T. J. H., & Salinger, M. J. (2002). Interannual variation in end-of-summer snowlines of the Southern Alps of New Zealand, and relationships with Southern Hemisphere atmospheric circulation and sea surface temperature patterns. *International Journal of Climatology*, *22*(1), 107–120. https://doi.org/10.1002/joc.722

Collier, E., & Immerzeel, W. W. (2015). High-resolution modeling of atmospheric dynamics in the Nepalese Himalaya. *Journal of Geophysical Research: Atmospheres*, *120*(19), 9882–9896. https://doi.org/10.1002/2015JD023266

Collier, E., Maussion, F., Nicholson, L. I., Mölg, T., Immerzeel, W. W., & Bush, A. B. G. (2015). Impact of debris cover on glacier ablation and atmosphere-glacier feedbacks in the Karakoram. *The Cryosphere*, *9*(4), 1617–1632. https://doi.org/10.5194/tc-9-1617-2015

Collier, E., Mölg, T., & Sauter, T. (2018). Recent atmospheric variability at Kibo Summit, Kilimanjaro, and its relation to climate mode activity. *Journal of Climate*, *31*(10), 3875–3891. https://doi.org/10.1175/JCLI-D-17-0551.1

Conway, J. P., & Cullen, N. J. (2013). Constraining turbulent heat flux parameterization over a temperate maritime glacier in New Zealand. *Annals of Glaciology*, *54*(63), 41–51. https://doi.org/10.3189/2013AoG63A604

Conway, J. P., & Cullen, N. J. (2016). Cloud effects on surface energy and mass balance in the ablation area of Brewster Glacier, New Zealand. *The Cryosphere*, *10*(1), 313–328. https://doi.org/10.5194/tc-10-313-2016

Conway, J. P., Cullen, N. J., Spronken-Smith, R. A., & Fitzsimons, S. J. (2015). All-sky radiation over a glacier surface in the Southern Alps of New Zealand: Characterizing cloud effects on incoming shortwave, longwave and net radiation. *International Journal of Climatology*, *35*(5), 699–713. https://doi.org/10.1002/joc.4014

Cullen, N. J., & Conway, J. P. (2015). A 22-month record of surface meteorology and energy balance from the ablation zone of Brewster Glacier, New Zealand. *Journal of Glaciology*, *61*(229), 931–946. https://doi.org/10.3189/2015JoG15J004

Cullen, N. J., Gibson, P. B., Mölg, T., Conway, J. P., Sirguey, P., & Kingston, D. G. (2019). The influence of weather systems in controlling mass balance in the Southern Alps of New Zealand. *Journal of Geophysical Research: Atmospheres*, *124*(8), 4514–4529. https://doi.org/10.1029/2018JD030052

Doyle, J. D. (1997). The influence of mesoscale orography on a coastal jet and rainband. *Monthly Weather Review*, *125*(7), 1465–1488. https://doi.org/10.1175/1520-0493(1997)125<1465:TIOMOO>2.0.CO;2

Doyle, J. D., & Bond, N. A. (2001). Research aircraft observations and numerical simulations of a warm front approaching Vancouver Island. *Monthly Weather Review*, *129*(5), 978–998. https://doi.org/10.1175/1520-0493(2001)129<0978:RAOANS>2.0.CO;2

Dudhia, J. (1989). Numerical study of convection observed during the winter monsoon experiment using a mesoscale two-dimensional model. *Journal of the Atmospheric Sciences*, *46*(20), 3077–3107. https://doi.org/10.1175/1520-0469(1989)046<3077:NSOCOD>2.0.CO;2

Durran, D. R. (1990). Mountain waves and downslope winds. In W. Blumen (Ed.), Atmospheric Processes Over Complex Terrain, Meteorological Monographs (Vol. 23, pp. 59–81). American Meteorological Society.

Durran, D. R., & Klemp, J. B. (1982). On the effects of moisture on the Brunt-Väisälä frequency. *Journal of the Atmospheric Sciences*, *39*(10), 2152–2158. https://doi.org/10.1175/1520-0469(1982)039<2152:OTEOMO>2.0.CO;2

Elvidge, A. D., & Renfrew, I. A. (2016). The causes of foehn warming in the lee of mountains. *Bulletin of the American Meteorological Society*, *97*(3), 455–466. https://doi.org/10.1175/BAMS-D-14-00194.1

Elvidge, A. D., Renfrew, I. A., King, J. C., Orr, A., & Lachlan-Cope, T. A. (2014). Foehn warming distributions in nonlinear and linear flow regimes: A focus on the Antarctic Peninsula. *Quarterly Journal of the Royal Meteorological Society*, *142*(695), 618–631. https://doi.org/10.1002/qj.2489

Finlon, J. A., Rauber, R. M., Wu, W., Zaremba, T. J., McFarquhar, G. M., Nesbitt, S. W., et al. (2020). Structure of an atmospheric river over Australia and the Southern Ocean: II. Microphysical evolution. *Journal of Geophysical Research: Atmospheres*, *125*(18), e2020JD032514. https://doi.org/10.1029/2020JD032514

Fitzharris, B. B. (2001). Global energy and climate processes. In A. P. Sturman, & R. A. Spronken-Smith (Eds.), *The Physical Environment: A New Zealand Perspective* (pp. 62–75). Oxford University Press.

Fitzharris, B. B., Chinn, T. J. H., & Lamont, G. N. (1997). Glacier balance fluctuations and atmospheric patterns over the Southern Alps, New Zealand. *International Journal of Climatology*, *17*(7), 1–19. https://doi.org/10.1002/(SICI)1097-0088(19970615)17:7<745::AID-JOC160>3.0.CO;2-Y

Fitzharris, B. B., Clare, G. R., & Renwick, J. (2007). Teleconnections between Andean and New Zealand glaciers. *Global and Planetary Change*, *59*(1–4), 159–174. https://doi.org/10.1016/j.gloplacha.2006.11.022

Fitzharris, B. B., Hay, J. E., & Jones, P. D. (1992). Behavior of New Zealand glaciers and atmospheric circulation changes over the past 130 years. *The Holocene*, *2*(2), 97–106. https://doi.org/10.1177/095968369200200201

Fuhrer, O., & Schär, C. (2005). Embedded cellular convection in moist flow past topography. *Journal of the Atmospheric Sciences*, *62*(8), 2810–2828. https://doi.org/10.1175/JAS3512.1

Gardelle, J., Berthier, E., Arnaud, Y., & Kääb, A. (2013). Region-wide glacier mass balances over the Pamir-Karakoram-Himalaya during 1999–2011. *The Cryosphere*, *7*(4), 1263–1286. https://doi.org/10.5194/tc-7-1263-2013

Gillett, S., & Cullen, N. J. (2011). Atmospheric controls on summer ablation over Brewster Glacier, New Zealand. *International Journal of Climatology*, *31*(13), 2033–2048. https://doi.org/10.1002/joc.2216

Gimeno, L., Nieto, R., Vázquez, M., & Lavers, D. A. (2014). Atmospheric rivers: A mini-review. *Frontiers of Earth Science*, *2*(2), 1–6. https://doi.org/10.3389/feart.2014.00002

Gómez-Navarro, J. J., Raible, C. C., & Dierer, S. (2015). Sensitivity of the WRF model to PBL parametrisations and nesting techniques: Evaluation of wind storms over complex terrain. *Geoscientific Model Development*, *8*(10), 3349–3363. https://doi.org/10.5194/gmd-8-3349-2015

Griffiths, G. A., & McSaveney, M. J. (1983). Distribution of mean annual precipitation across some steepland regions of New Zealand. *New Zealand Journal of Science*, *26*(2), 197–209.

Guan, B., & Waliser, D. E. (2015). Detection of atmospheric rivers: evaluation and application of an algorithm for global studies. *Journal of Geophysical Research: Atmospheres*, *120*(24), 514–535. https://doi.org/10.1002/2015JD024257

Hay, J. E., & Fitzharris, B. B. (1988). The synoptic climatology of ablation on a New Zealand glacier. *Journal of Climatology*, *8*(2), 201–215. https://doi.org/10.1002/joc.3370080207

Hersbach, H., Bell, B., Berrisford, P., Hirahara, S., Horányi, A., Muñoz-Sabater, J., et al. (2020). The ERA5 global reanalysis. *Quarterly Journal of the Royal Meteorological Society*, *146*(730), 1999–2049. https://doi.org/10.1002/qj.3803

Hoelzle, M., Chinn, T., Stumm, D., Paul, F., Zemp, M., & Haeberli, W. (2007). The application of glacier inventory data for estimating past climate change effects on mountain glaciers: A comparison between the European Alps and the Southern Alps of New Zealand. *Global and Planetary Change*, *56*(1–2), 69–82. https://doi.org/10.1016/j.gloplacha.2006.07.001

Hoinka, K. P. (1985). What is a foehn clearance? *Bulletin of the American Meteorological Society*, *66*(9), 1123–1132. https://doi.org/10.1175/1520-0477(1985)066<1123:WIAFC>2.0.CO;2

Hong, S.-Y., Noh, Y., & Dudhia, J. (2006). A new vertical diffusion package with an explicit treatment of entrainment processes. *Monthly Weather Review*, *134*(9), 2318–2341. https://doi.org/10.1175/MWR3199.1

Houze, R. A., Jr. (1993). *Cloud dynamics*. Academic.

Houze, R. A., Jr., & Medina, S. (2005). Turbulence as a mechanism for orographic precipitation enhancement. *Journal of the Atmospheric Sciences*, *62*(10), 3599–3623. https://doi.org/10.1175/JAS3555.1

Iacono, M. J., Delamere, J. S., Mlawer, E. J., Shephard, M. W., Clough, S. A., & Collins, W. D. (2008). Radiative forcing by long-lived greenhouse gases: Calculations with the AER radiative transfer models. *Journal of Geophysical Research*, *113*(D13), D13103. https://doi.org/10.1029/2008JD009944

Jarvis, A., Guevara, E., Reuter, H. I., & Nelson, A. D. (2008). *Hole-filled SRTM for the globe: Version 4: Data grid* (Web publication/site). Retrieved from University of Twente Research Information http://srtm.csi.cgiar.org/. CGIAR Consortium for Spatial Information.

Jiménez, P. A., Dudhia, J., González-Rouco, J. F., Navarro, J., Montávez, J. P., & García-Bustamante, E. (2012). A revised scheme for the WRF surface layer formulation. *Monthly Weather Review*, *140*(3), 898–918. https://doi.org/10.1175/MWR-D-11-00056.1

Kain, J. S. (2004). The Kain-Fritsch convective parameterization: An update. *Journal of Applied Meteorology*, *43*(1), 170–181. https://doi.org/10.1175/1520-0450(2004)043<0170:TKCPAU>2.0.CO;2

Katzfey, J. J. (1995). Simulation of extreme New Zealand precipitation events. Part I: Sensitivity to orography and resolution. *Monthly Weather Review*, *123*(3), 737–754. https://doi.org/10.1175/1520-0493(1995)123<0737:SOENZP>2.0.CO;2

King, J. C., Kirchgaessner, A., Bevan, S., Elvidge, A. D., Kuipers Munneke, P., Luckman, A., et al. (2017). The impact of foehn winds on surface energy balance during the 2010–2011 melt season over Larsen C Ice Shelf, Antarctica. *Journal of Geophysical Research: Atmospheres*, *122*(22), 12062–12076. https://doi.org/10.1002/2017JD026809

Kingston, D. G., Lavers, D. A., & Hannah, D. M. (2016). Floods in the Southern Alps of New Zealand: The importance of atmospheric rivers. *Hydrological Processes*, *30*(26), 5063–5070. https://doi.org/10.1002/hyp.10982

Kirshbaum, D. J., & Durran, D. R. (2004). Factors governing cellular convection in orographic precipitation. *Journal of the Atmospheric Sciences*, *61*(6), 682–698. https://doi.org/10.1175/1520-0469(2004)061<0682:FGCCIO>2.0.CO;2

Klemp, J. B., & Lilly, D. R. (1975). The dynamics of wave-induced downslope winds. *Journal of the Atmospheric Sciences*, *32*(2), 320–339. https://doi.org/10.1175/1520-0469(1975)032<0320:TDOWID>2.0.CO;2

Little, K., Kingston, D. G., Cullen, N. J., & Gibson, P. B. (2019). The role of atmospheric rivers for extreme ablation and snowfall events in the Southern Alps of New Zealand. *Geophysical Research Letters*, *46*(5), 2761–2771. https://doi.org/10.1029/2018GL081669

Mackintosh, A. N., Anderson, B. M., Lorrey, A. M., Renwick, J. A., Frei, P., & Dean, S. M. (2017). Regional cooling caused recent New Zealand glacier advances in a period of global warming. *Nature Communications*, *8*, 14202. https://doi.org/10.1038/ncomms14202

Marcus, M. G., Moore, R. D., & Owens, I. F. (1985). Short-term estimates of surface energy transfers and ablation on the lower Franz Josef Glacier, South Westland, New Zealand. *New Zealand Journal of Geology and Geophysics*, *28*(3), 559–567. https://doi.org/10.1080/00288306.1985.10421208

Marzeion, B., Cogley, J. G., Richter, K., & Parkes, D. (2014). Attribution of global glacier mass loss to anthropogenic and natural causes. *Science*, *345*(6199), 919–921. https://doi.org/10.1126/science.1254702

McCauley, M. P., & Sturman, A. P. (1999). A study of orographic blocking and barrier wind development upstream of the Southern Alps, New Zealand. *Meteorology and Atmospheric Physics*, *70*(3), 121–131. https://doi.org/10.1007/s007030050029

McGowan, H. A., & Sturman, A. P. (1996). Regional and local scale characteristics of foehn wind events over the South Island of New Zealand. *Meteorology and Atmospheric Physics*, *58*(1–4), 151–164. https://doi.org/10.1007/BF01027562

McGowan, H. A., Sturman, A. P., Kossmann, M., & Zawar-Reza, P. (2002). Observations of foehn onset in the Southern Alps, New Zealand. *Meteorology and Atmospheric Physics*, *79*(3–4), 215–230. https://doi.org/10.1007/s007030200004

McGowan, H. A., Sturman, A. P., & Owens, I. F. (1996). Aeolian dust transport and deposition by foehn winds in an alpine environment, Lake Tekapo, New Zealand. *Geomorphology*, *15*(2), 135–146. https://doi.org/10.1016/0169-555X(95)00123-M

Medina, S., & Houze, R. A., Jr. (2003). Air motions and precipitation growth in alpine storms. *Quarterly Journal of the Royal Meteorological Society*, *129*(588), 345–371. https://doi.org/10.1256/qj.02.13

Miglietta, M. M., & Buzzi, A. (2001). A numerical study of moist stratified flows over isolated topography. *Tellus A: Dynamic Meteorology and Oceanography*, *53*(4), 481–499. https://doi.org/10.3402/tellusa.v53i4.12222

Miglietta, M. M., & Rotunno, R. (2005). Simulations of moist nearly neutral flow over a ridge. *Journal of the Atmospheric Sciences*, *62*(5), 1410–1427. https://doi.org/10.1175/JAS3410.1

Mölg, T., Cullen, N. J., Hardy, D. R., Kaser, G., & Klok, L. (2008). Mass balance of a slope glacier on Kilimanjaro and its sensitivity to climate. *International Journal of Climatology*, *28*(7), 881–892. https://doi.org/10.1002/joc.1589

Mölg, T., Cullen, N. J., Hardy, D. R., Winkler, M., & Kaser, G. (2009). Quantifying climate change in the tropical midtroposphere over East Africa from glacier shrinkage on Kilimanjaro. *Journal of Climate*, *22*(15), 4162–4181. https://doi.org/10.1175/2009JCLI2954.1

Mölg, T., & Kaser, G. (2011). A new approach to resolving climate–cryosphere relations: Downscaling climate dynamics to glacier-scale mass and energy balance without statistical scale linking. *Journal of Geophysical Research*, *116*(D16), D16101. https://doi.org/10.1029/2011JD015669

Mölg, T., Maussion, F., Collier, E., Chiang, J. C. H., & Scherer, D. (2017). Prominent midlatitude circulation signature in High Asia's surface climate during monsoon. *Journal of Geophysical Research: Atmospheres*, *122*(23), 12702–12712. https://doi.org/10.1002/2017JD027414

Morrison, H., Thompson, G., & Tatarskii, V. (2009). Impact of cloud microphysics on the development of trailing stratiform precipitation in a simulated squall line: Comparison of one- and two-moment schemes. *Monthly Weather Review*, *137*(3), 991–1007. https://doi.org/10.1175/2008MWR2556.1

Neale, S. M., & Fitzharris, B. B. (1997). Energy balance and synoptic climatology of a melting snowpack in the Southern Alps, New Zealand. *International Journal of Climatology*, *17*(14), 1595–1609. https://doi.org/10.1002/(SICI)1097-0088(19971130)17:14<1595::AID-JOC213>3.0.CO;2-7

Neiman, P. J., Ralph, F. M., White, A. B., Kingsmill, D. E., & Persson, P. O. G. (2002). The statistical relationship between upslope flow and rainfall in California's Coastal Mountains: Observations during CALJET. *Monthly Weather Review*, *130*(6), 1468–1492. https://doi.org/10.1175/1520-0493(2002)130<1468:TSRBUF>2.0.CO;2

Neiman, P. J., Ralph, F. M., Wick, G. A., Kuo, Y.-H., Wee, T.-K., Ma, Z., et al. (2008). Diagnosis of an intense atmospheric river impacting the Pacific Northwest: Storm summary and offshore vertical structure observed with COSMIC satellite retrievals. *Monthly Weather Review*, *136*(11), 4398–4420. https://doi.org/10.1175/2008MWR2550.1

Neiman, P. J., Schick, L. J., Ralph, F. M., Hughes, M., & Wick, G. A. (2011). Flooding in Western Washington: The connection to atmospheric rivers*. *Journal of Hydrometeorology*, *12*(6), 1337–1358. https://doi.org/10.1175/2011JHM1358.1

Niu, G.-Y., Yang, Z.-L., Mitchell, K. E., Chen, F., Ek, M. B., Barlage, M., et al. (2011). The community Noah land surface model with multiparameterization options (Noah-MP): 1. Model description and evaluation with local-scale measurements. *Journal of Geophysical Research*, *116*(D12), D12109. https://doi.org/10.1029/2010JD015140

Nye, J. F. (1960). The response of glaciers and ice-sheets to seasonal and climatic changes. *Proceedings of the Royal Society A: Mathematical, Physical and Engineering Sciences*, *256*(1287), 559–584. https://doi.org/10.1098/rspa.1960.0127

Olauson, J. (2018). ERA5: The new champion of wind power modeling? *Renewable Energy*, *126*, 322–331. https://doi.org/10.1016/j.renene.2018.03.056

Orr, A., Listowski, C., Couttet, M., Collier, E., Immerzeel, W., Deb, P., & Bannister, D. (2017). Sensitivity of simulated summer monsoonal precipitation in Langtang Valley, Himalaya, to cloud microphysics schemes in WRF. *Journal of Geophysical Research: Atmospheres*, *122*(12), 6298–6318. https://doi.org/10.1002/2016JD025801

Overland, J. E., & Bond, N. A. (1995). Observations and scale analysis of coastal wind jets. *Monthly Weather Review*, *123*(10), 2934–2941. https://doi.org/10.1175/1520-0493(1995)123<2934:OASAOC>2.0.CO;2

Parish, T. R. (1982). Barrier winds along the Sierra Nevada mountains. *Journal of Applied Meteorology*, *21*(7), 925–930. https://doi.org/10.1175/1520-0450(1982)021<0925:BWATSN>2.0.CO;2

Pfeffer, W. T., Arendt, A. A., Bliss, A., Bolch, T., Cogley, J. G., Gardner, A. S., et al. (2014). The Randolph Glacier Inventory: A globally complete inventory of glaciers. *Journal of Glaciology*, *60*(221), 537–552. https://doi.org/10.3189/2014JoG13J176

Pierrehumbert, R. T., & Wyman, B. (1985). Upstream effects of mesoscale mountains. *Journal of the Atmospheric Sciences*, *42*(10), 977–1003. https://doi.org/10.1175/1520-0469(1985)042<0977:UEOMM>2.0.CO;2

Prince, H. D. (2020). *A Climatology of New Zealand atmospheric rivers* (Master's thesis). University of Otago. Retrieved from University of Otago Library Archive http://hdl.handle.net/10523/10221

Prince, H. D., Cullen, N. J., Gibson, P. B., Conway, J., & Kingston, D. G. (2021). A climatology of atmospheric rivers in New Zealand. *Journal of Climate*, Early Online Release, 1–56. https://doi.org/10.1175/JCLI-D-20-0664.1

Purdie, H. L., Brook, M. S., & Fuller, I. C. (2008). Seasonal variation in ablation and surface velocity on a temperate maritime glacier: Fox Glacier, New Zealand. *Arctic Antarctic and Alpine Research*, *40*(1), 140–147. https://doi.org/10.1657/1523-0430(06-032)[PURDIE]2.0.CO;2

Purdie, H. L., Mackintosh, A., Lawson, W., & Anderson, B. (2011). Synoptic influences on snow accumulation on glaciers east and west of a topographic divide: Southern Alps, New Zealand. *Arctic Antarctic and Alpine Research*, *43*(1), 82–94. https://doi.org/10.1657/1938-4246-43.1.82

Purdy, J. C., & Austin, G. L. (2003). The role of synoptic cloud in orographic rainfall in the Southern Alps of New Zealand. *Meteorological Applications*, *10*(4), 355–365. https://doi.org/10.1017/S1350482703001087

Purdy, J. C., Austin, G. L., Seed, A. W., & Cluckie, I. D. (2005). Radar evidence of orographic enhancement due to the seeder feeder mechanism. *Meteorological Applications*, *12*(3), 199–206. https://doi.org/10.1017/S1350482705001672

Ralph, F. M., & Dettinger, M. D. (2011). Storms, floods, and the science of atmospheric rivers. *Eos Transactions American Geophysical Union*, *92*(32), 265–266. https://doi.org/10.1029/2011EO320001

Ralph, F. M., Dettinger, M. D., Cairns, M. M., Galarneau, T. J., & Eylander, J. (2018). Defining "atmospheric river": How the glossary of meteorology helped resolve a debate. *Bulletin of the American Meteorological Society*, *99*(4), 837–839. https://doi.org/10.1175/BAMS-D-17-0157.1

Ralph, F. M., Iacobellis, S. F., Neiman, P. J., Cordeira, J. M., Spackman, J. R., Waliser, D. E., et al. (2017). Dropsonde observations of total integrated water vapor transport within North Pacific atmospheric rivers. *Journal of Hydrometeorology*, *18*(9), 2577–2596. https://doi.org/10.1175/JHM-D-17-0036.1

Ralph, F. M., Neiman, P. J., & Rotunno, R. (2005). Dropsonde observations in low-level jets over the Northeastern Pacific Ocean from CALJET-1998 and PACJET-2001: Mean vertical-profile and atmospheric-river characteristics. *Monthly Weather Review*, *133*(4), 889–910. https://doi.org/10.1175/MWR2896.1

Ralph, F. M., Neiman, P. J., & Wick, G. A. (2004). Satellite and CALJET aircraft observations of atmospheric rivers over the Eastern North Pacific Ocean during the winter of 1997/98. *Monthly Weather Review*, *132*(7), 1721–1745. https://doi.org/10.1175/1520-0493(2004)132<1721:SACAOO>2.0.CO;2

Ralph, F. M., Rutz, J. J., Cordeira, J. M., Dettinger, M. D., Anderson, M., Reynolds, D., et al. (2019). A scale to characterize the strength and impacts of atmospheric rivers: A scale for atmospheric river intensity and potential impacts is introduced, enhancing situational awareness and forecast communication. *Bulletin of the American Meteorological Society*, *100*(2), 69–89. https://doi.org/10.1175/BAMS-D-18-0023.1

Rauber, R. M., Hu, H., Dominguez, F., Nesbitt, S. W., McFarquhar, G. M., Zaremba, T. J., & Finlon, J. A. (2020). Structure of an atmospheric river over Australia and the Southern Ocean. Part I: Tropical and midlatitude water vapor fluxes. *Journal of Geophysical Research: Atmospheres*, *125*(18), e2020JD032513. https://doi.org/10.1029/2020JD032513

Revell, M. J., Copeland, J. H., Larsen, H. R., & Wratt, D. S. (2002). Barrier jets around the Southern Alps of New Zealand and their potential to enhance alpine rainfall. *Atmospheric Research*, *61*(4), 277–298. https://doi.org/10.1016/S0169-8095(01)00142-9

Richner, H., Baumann-Stanzer, K., Benech, B., Berger, H., Chimani, B., Dorninger, M., et al. (2006). Unstationary aspects of foehn in a large valley part I: Operational setup, scientific objectives and analysis of the cases during the special observing period of the MAP subprogramme FORM. *Meteorology and Atmospheric Physics*, *92*(3), 255–284. https://doi.org/10.1007/s00703-005-0134-y

Rosier, S., Dean, S., Stuart, S., Carey-Smith, T., Black, M. T., & Massey, N. (2015). Extreme rainfall in early July 2014 in Northland, New Zealand – Was there an anthropogenic influence? *Bulletin of the American Meteorological Society*, *96*(12), 136–140. https://doi.org/10.1175/BAMS-D-15-00105.1

Rotunno, R., & Houze, R. A. (2007). Lessons on orographic precipitation from the Mesoscale Alpine Programme. *Quarterly Journal of the Royal Meteorological Society*, *133*(625), 811–830. https://doi.org/10.1002/qj.67

Salinger, M. J., Fitzharris, B. B., & Chinn, T. (2019). Atmospheric circulation and ice volume changes for the small and medium glaciers of New Zealand's Southern Alps mountain range 1977-2018. *International Journal of Climatology*, *39*(11), 4274–4287. https://doi.org/10.1002/joc.6072

Sauter, T. (2020). Revisiting extreme precipitation amounts over southern South America and implications for the Patagonian Icefields. *Hydrology and Earth System Sciences*, *24*(4), 2003–2016. https://doi.org/10.5194/hess-24-2003-2020

Schaefer, M., Machguth, H., Falvey, M., Casassa, G., & Rignot, E. (2015). Quantifying mass balance processes on the Southern Patagonia Icefield. *The Cryosphere*, *9*(1), 25–35. https://doi.org/10.5194/tc-9-25-2015

Schwerdtfeger, W. (1975). The effect of the Antarctic Peninsula on the temperature regime of the Weddell Sea. *Monthly Weather Review*, *103*(1), 45–51. https://doi.org/10.1175/1520-0493(1975)103<0045:TEOTAP>2.0.CO;2

Sharifi, E., Eitzinger, J., & Dorigo, W. (2019). Performance of the state-of-the-art gridded precipitation products over mountainous terrain: A regional study over Austria. *Remote Sensing*, *11*(17). https://doi.org/10.3390/rs11172018

Sinclair, M. R., Wratt, D. S., Henderson, R. D., & Gray, W. R. (1997). Factors affecting the distribution and spillover of precipitation in the Southern Alps of New Zealand: A case study. *Journal of Applied Meteorology*, *36*(5), 428–442. https://doi.org/10.1175/1520-0450(1997)036<0428:FATDAS>2.0.CO;2

Sirguey, P., Still, H., Cullen, N. J., Dumont, M., Arnaud, Y., & Conway, J. P. (2016). Reconstructing the mass balance of Brewster Glacier, New Zealand, using MODIS-derived glacier-wide albedo. *The Cryosphere*, *10*(5), 2465–2484. https://doi.org/10.5194/tc-10-2465-2016

Skamarock, W. C., Klemp, J. B., Dudhia, J., Gill, D. O., Zhiquan, L., Berner, J., et al. (2019). A description of the advanced research WRF model version 4. In *NCAR Technical Notes (No. NCAR/TN-556+STR)*. National Center for Atmospheric Research. https://doi.org/10.5065/1dfh-6p97

Smith, R. B. (1979). The Influence of Mountains on the Atmosphere. *Advances in Geophysics*, *21*, 87–230. https://doi.org/10.1016/S0065-2687(08)60262-9

Smith, R. B. (1980). Linear theory of stratified hydrostatic flow past an isolated mountain. *Tellus*, *32*(4), 348–364. https://doi.org/10.1111/j.2153-3490.1980.tb00962.x

Temme, F., Turton, J. V., Mölg, T., & Sauter, T. (2020). Flow regimes and föhn types characterize the local climate of Southern Patagonia. *Atmosphere*, *11*(9), 899. https://doi.org/10.3390/atmos11090899

Trachsel, M., & Nesje, A. (2015). Modeling annual mass balances of eight Scandinavian glaciers using statistical models. *The Cryosphere*, *9*(4), 1401–1414. https://doi.org/10.5194/tc-9-1401-2015

Turton, J. V., Kirchgaessner, A., Ross, A. N., & King, J. C. (2017). Does high-resolution modeling improve the spatial analysis of föhn flow over the Larsen C Ice Shelf? *Weather*, *72*(7), 192–196. https://doi.org/10.1002/wea.3028

Turton, J. V., Mölg, T., & Collier, E. (2020). High-resolution (1 km) Polar WRF output for 79°N Glacier and the northeast of Greenland from 2014 to 2018. *Earth System Science Data*, *12*(2), 1191–1202. https://doi.org/10.5194/essd-12-1191-2020

Viale, M., Houze, R. A., Jr., & Rasmussen, K. L. (2013). Upstream orographic enhancement of a narrow cold-frontal rainband approaching the Andes. *Monthly Weather Review*, *141*(5), 1708–1730. https://doi.org/10.1175/MWR-D-12-00138.1

Waliser, D., & Guan, B. (2017). Extreme winds and precipitation during landfall of atmospheric rivers. *Nature Geoscience*, *10*, 179–183. https://doi.org/10.1038/ngeo2894

Weisman, M. L., Skamarock, W. C., & Klemp, J. B. (1997). The resolution dependence of explicitly modeled convective systems. *Monthly Weather Review*, *125*(4), 527–548. https://doi.org/10.1175/1520-0493(1997)125<0527:TRDOEM>2.0.CO;2

WGMS. (2008). *Global Glacier Changes: facts and figures*. World Glacier Monitoring Service.

Wille, J. D., Favier, V., Dufour, A., Gorodetskaya, I. V., Turner, J., Agosta, C., & Codron, F. (2019). West Antarctic surface melt triggered by atmospheric rivers. *Nature Geoscience*, *12*, 911–916. https://doi.org/10.1038/s41561-019-0460-1

Willsman, A. P., Chinn, T. J., & Macara, G. (2015). New Zealand Glacier Monitoring: End of summer snowline survey 2015. In *NIWA Client Reports (No. CHC2015-122)*. National Institute of Water & Atmospheric Research Ltd.

Wratt, D. S., Revell, M. J., Sinclair, M. R., Gray, W. R., Henderson, R. D., & Chater, A. M. (2000). Relationships between air mass properties and mesoscale rainfall in New Zealand's Southern Alps. *Atmospheric Research*, *52*(4), 261–282. https://doi.org/10.1016/S0169-8095(99)00038-1

Wratt, D. S., Ridley, R. N., Sinclair, M. R., Larsen, H., Thompson, S. M., Henderson, R., et al. (1996). The New Zealand Southern Alps experiment. *Bulletin of the American Meteorological Society*, *77*(4), 683–692. https://doi.org/10.1175/1520-0477(1996)077<0683:TNZSAE>2.0.CO;2

Yeh, H.-C., & Chen, Y.-L. (2003). Numerical simulations of the barrier jet over Northwestern Taiwan during the Mei-Yu season. *Monthly Weather Review*, *131*(7), 1396–1407. https://doi.org/10.1175/1520-0493(2003)131<1396:NSOTBJ>2.0.CO;2

Zängl, G. (2012). Extending the numerical stability limit of terrain-following coordinate models over steep slopes. *Monthly Weather Review*, *140*(11), 3722–3733. https://doi.org/10.1175/MWR-D-12-00049.1

Zhang, H., Pu, Z., & Zhang, X. (2013). Examination of errors in near-surface temperature and wind from WRF numerical simulations in regions of complex terrain. *Weather and Forecasting*, *28*(3), 893–914. https://doi.org/10.1175/WAF-D-12-00109.1

Zhu, Y., & Newell, R. E. (1998). A proposed algorithm for moisture fluxes from atmospheric rivers. *Monthly Weather Review*, *126*(3), 725–735. https://doi.org/10.1175/1520-0493(1998)126<0725:APAFMF>2.0.CO;2